Czech Technical University in Prague
Faculty of Electrical Engineering
Department of Circuit Theory

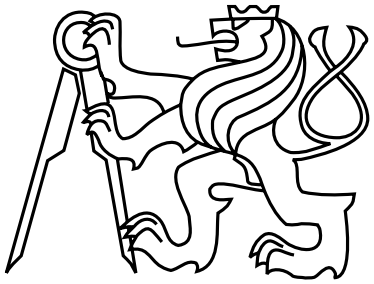

Optimization of sound absorption in rectangular acoustic black holes

Bachelor's Thesis

Aneta Furmanová

Supervisor: RNDr. MgA. Viktor Hruška, Ph.D.

Study Programme: Lékařská elektronika a bioinformatika, Bakalářský

Prague, May 12, 2023

BACHELOR‘S THESIS ASSIGNMENT

I. Personal and study details

Student's name: **Furmanová Aneta** Personal ID number: **499125**

Faculty / Institute: **Faculty of Electrical Engineering**

Department / Institute: **Department of Circuit Theory**

Study program: **Medical Electronics and Bioinformatics**

II. Bachelor’s thesis details

Bachelor’s thesis title in English:

Optimization of sound absorption in rectangular acoustic black holes

Bachelor’s thesis title in Czech:

Optimization of sound absorption in rectangular acoustic black holes

Guidelines:

Acoustic black holes (ABH) are devices designed to slow down the phase velocity of incoming waves. As a result, there is a significant increase in acoustic energy density and hence the importance of weaker dissipation mechanism grows. The aim of this thesis is to investigate the possibilities of optimizing the ABH geometry in order to maximize the absorption of incoming acoustic waves.
1) Study the relevant literature (see the list below).
2) Implement the governing equation for ABH reflection coefficient in Python. Specifically, employ the modules SciPy and NumPy to integrate the corresponding nonlinear differential equation of Riccati type).
3) Use Bezier curves of general order to extend the possible geometries.
4) Employ a suitable optimization algorithm to find the best geometries for various requirements (e.g. for overall absorption, with preference of lower frequencies etc.)
5) Discuss the impact of each type of acoustic dissipative losses and suggest possible future research directions.

Bibliography / sources:

- Blackstock. Fundamentals of Physical Acoustics. Wiley, 2000
- Jimenéz, Umnova, Groby. Acoustic Waves in Periodic Structires, Metamaterials and Porous Media. Springer, 2021.
- PELAT, GAUTIER, CONLON and SEMPERLOTTI. The acoustic black hole: A review of theory and applications. Journal of Sound and Vibration. 2020, 476

Name and workplace of bachelor’s thesis supervisor:

RNDr. MgA. Viktor Hruška, Ph.D. Department of Physics FEE

Name and workplace of second bachelor’s thesis supervisor or consultant:

Date of bachelor’s thesis assignment: **23.01.2023** Deadline for bachelor thesis submission: **26.05.2023**

Assignment valid until: **22.09.2024**

RNDr. MgA. Viktor Hruška, Ph.D.	doc. Ing. Radoslav Bortel, Ph.D.	prof. Mgr. Petr Páta, Ph.D.
Supervisor’s signature	Head of department’s signature	Dean’s signature

III. Assignment receipt

The student acknowledges that the bachelor’s thesis is an individual work. The student must produce her thesis without the assistance of others, with the exception of provided consultations. Within the bachelor’s thesis, the author must state the names of consultants and include a list of references.

.	
Date of assignment receipt	Student’s signature

Aknowledgements

I would like to thank my supervisor Viktor Hruška for the guidance, advice and patience. Most of all, I am grateful for the knowledge, experience and opportunities I was given. I would also like to thank my family for their support.

Declaration

I declare that I elaborated this thesis on my own and that I mentioned all the information sources and literature that have been used in accordance with the Guideline for adhering to ethical principles in the course of elaborating an academic final thesis.

In Prague on May 12, 2023 .....

Abstract

This thesis deals with sound absorption optimization in rectangular acoustic black holes (ABH). Specifically, for the ABH in air realized as an anechoic termination to rectangular waveguides consisting of thin rectangular ribs embedded within the duct. By tuning the geometric parameters of ABHs, we aim to maximize sound absorption while keeping the parameters within the limits of practically feasible 3D printing with the current state of development. The equations of motion of compressible fluids are briefly reviewed, and their acoustical limit is discussed. It is shown how they can be transformed in the Riccati type of equation for the specific purpose of ABH. This quasi-onedimensional description is advantageous for employment in optimization.

In this work, we optimize the profile function of the ABH, which controls the height of the ribs. Due to the complicated relations within the system, a derivative-free optimization is needed. Hence, we have chosen the Covariance Matrix Adaptation Evolution Strategy. Two scenarios are studied in this work: a rectangular ABH with narrow slits filled with air and a combination of ABH with a porous material. The first scenario is useful for employment in extreme conditions (e.g., high temperature, humidity) or conditions with increased hygiene standards (healthcare industry). The latter aims to increase sound absorption in the frequency range where the porous materials do not operate ideally.

Keywords: sound absorption, acoustic black hole, porous materials, evolution strategy

Abstrakt

Tato práce se zabývá optimalizací absorpce zvuku v obdélníkových akustických černých dírách (ABH). Konkrétně pro ABH ve vzduchu realizovanou jako anechoické zakončení obdélníkových vlnovodů tvořených tenkými obdélníkovými žebry vloženými do kanálu. Laděním geometrických parametrů ABH se snažíme maximalizovat absorpci zvuku a zároveň udržet parametry v mezích prakticky proveditelného 3D tisku při současném stavu vývoje. Stručně se seznámíme s pohybovými rovnicemi stlačitelných tekutin a diskutujeme jejich akustické limity. Je ukázáno, jak je lze transformovat do rovnic Riccatiho typu pro konkrétní účely ABH. Tento kvazi-jednorozměrný popis je výhodný pro využití při optimalizaci.

V této práci optimalizujeme profilovou funkci ABH, která řídí výšku žeber. Vzhledem ke komplikovaným vztahům uvnitř systému je nutná bezderivační optimalizace. Proto jsme zvolili evoluční strategii s adaptací kovarianční matice. V této práci se zabýváme dvěma případy využití ABH: obdélníkovou ABH s úzkými štěrbinami vyplněnými vzduchem a kombinací ABH s porézním materiálem. První případ je vhodný pro použití v extrémních podmínkách (např. vysoká teplota, vlhkost) nebo v podmínkách se zvýšenými hygienickými standardy (zdravotnictví). Druhý případ má za cíl zvýšit absorpci zvuku ve frekvenčním pásmu, kde porézní materiály nepůsobí ideálně.

Klíčová slova: absorpce zvuku, akustická černá díra, porézní materiál, evoluční strategie

Contents

List of Figures

Chapter 1

Introduction

The negative impact of noise, particularly at low frequencies, has become a growing concern due to its harmful effects on health. Prolonged exposure to environmental noise is classified among the top environmental risks to health in Europe. Even though the levels of noise can be too low to cause biological damage to the ear, it can lead to non-auditory health effects such as annoyance, chronic sleep disturbance or ischaemic heart disease [1]. Therefore, there is a need for efficient structures able to suppress low-frequency sound.

So far, a widely used solution for noise and vibration control is use of porous materials, as they are able to dissipate vibro-acoustic energy through thermal and viscous losses. However, we are not able to use them in conditions with increased hygiene standards (healthcare industry), in extreme conditions (e.g., high temperatures, humidity), or due to their bulkiness and excess weight. Therefore, a need for other noise-reducing treatments emerged.

One of the possible solutions to this problem are passive devices suppressing the unwanted sound or vibration called acoustic black holes (ABHs). The ABHs can serve either as traps for flexural elastic waves in solid materials (also known as vibrational black holes) or for acoustic waves in air (sometimes called sonic black holes). However, the main principle remains the same [2]. Examples of both types are depicted in Figure 1.1. In this thesis, we will focus only on ABH for acoustic waves in fluids.

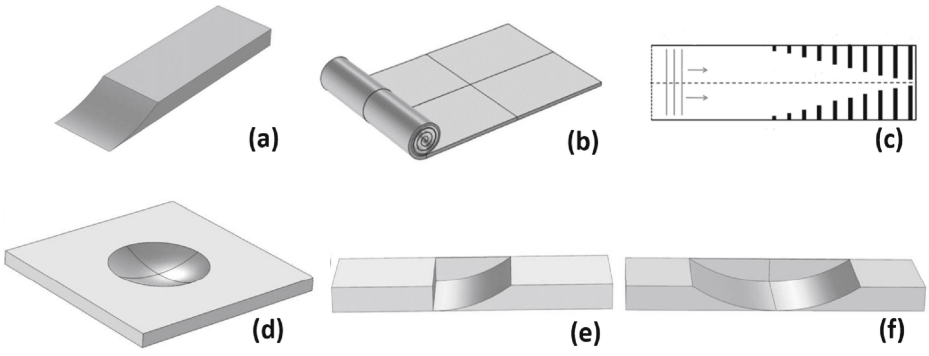

Figure 1.1: Examples of ABHs (from [2]). (a), (b), (c), (d), (e), (f) are vibrational black holes, (c) is a sonic black hole.

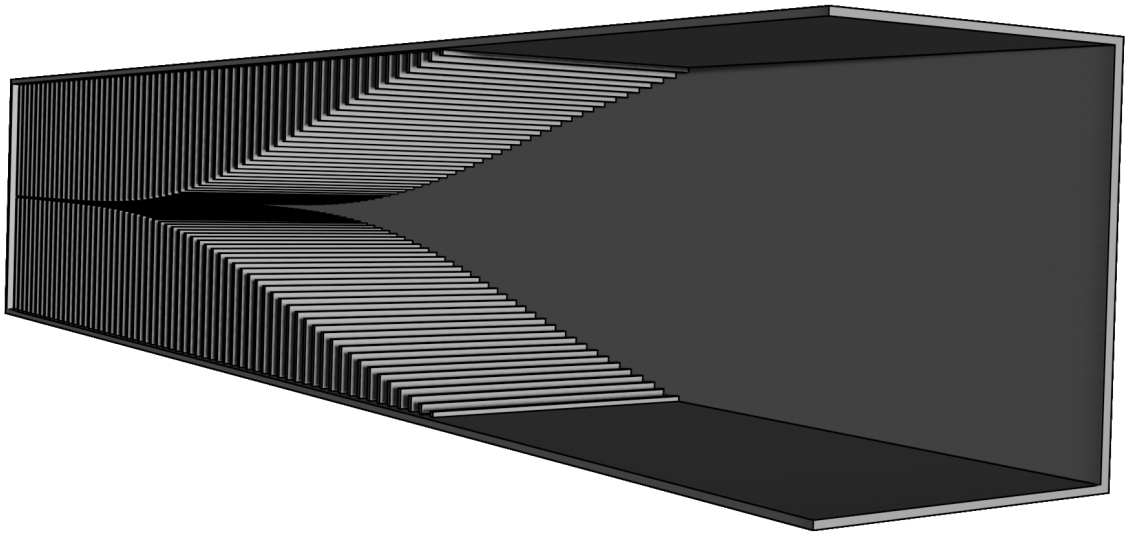

Figure 1.2: A three-dimensional render of a rectangular ABH.

The concept of a wave retarding structure was firstly proposed by Mironov and Pislyakov [3]. The underlying principle is that in this structure, the wave speed is reduced to zero; thus, the wave never reaches the end of the structure in a finite time. As a consequence, there is no reflection, and the wave remains simply trapped in the ABH. Hence, the nomenclature "black hole" based on astrophysics.

However, in the real world, the assumptions made for this theoretical model behaviour cannot be fulfilled. Thus, the black hole effect is not practically feasible, as was documented experimentally [4–7]. Therefore, for the sonic black holes, various authors avoid the term "black hole" and prefer other namings, such as "sound-absorbing structure" [8] or "metamaterial graded absorber" [9].

The ABHs studied in referred works have an axial symmetry and thus, can serve as termination for ducts with a circular cross-section. Throughout this work, we consider ABHs constructed as rectangular anechoic termination in air-filled waveguides with varying wall impedance. made with a collection of ribs of increasing heights. A cut of a three-dimensional render of considered rectangular ABH is depicted in Figure 1.2. In this thesis, two methods of rectangular ABHs usage are studied. Firstly, as absorbing structures in conditions where porous materials cannot be used. Secondly, as a way of improving the sound absorption in a frequency range where the porous material is not efficient enough.

In practice, the mechanism of losses in this structure is not due to the black hole effect. As the incoming wave propagates through the ABH, its group velocity is slowed down, and in turn, the wavelength is shortened, see Figure 1.3. This results in an increase of the acoustic energy density, which increases the effect of otherwise weak dissipation mechanisms, such as thermoviscous losses on the walls of ribs.

Our goal is to optimize the geometry of rectangular ABH in order to achieve better sound absorption. The quantitative description of the wave propagation in ABHs is based on the

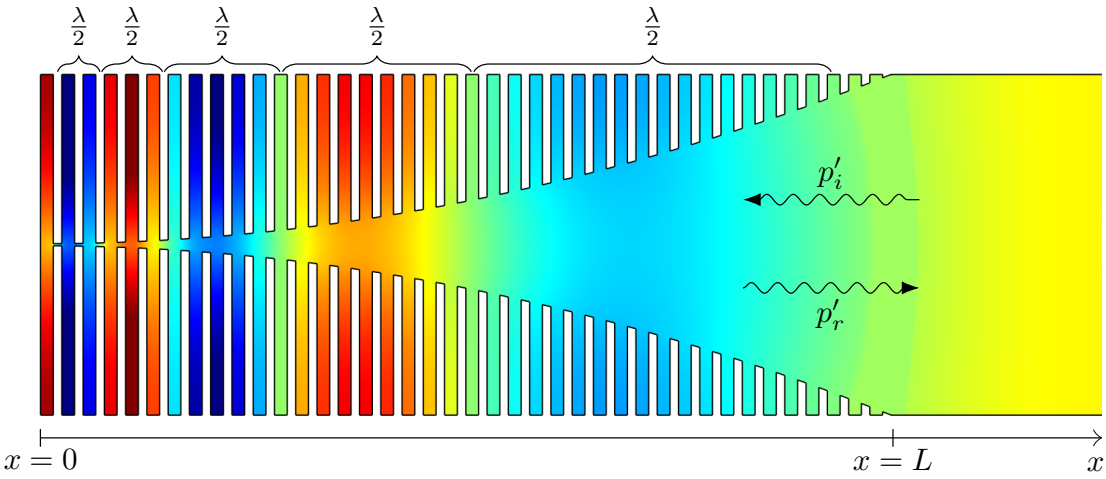

Figure 1.3: The wavelength tending to zero.

generalized Webster equation (see e.g. [10]). Since the generalized Webster equation for ABHs has a very limited amount of analytical solutions, some authors solved this problem by employing the finite element method (FEM) to solve the linearized Navier–Stokes equations (LNSE), which correctly captures thermoviscous losses [8, 11], while the authors of the papers [12, 13] used a one-dimensional model equation employing the transfer matrix method (TMM). However, none of these methods are suitable for use in optimization. The FEM because it is too computationally demanding. The TMM because it is complicated to express smooth geometry with it. It also does not provide us a governing equation and because a huge amount of matrices is needed for description of the ABH system, it is not possible to interpret the wave behaviour inside the system even in limit cases. It is well-known that a whole class of wave equations for acoustic pressure with spatial inhomogeneity can be transformed into the Riccati equation (see e.g. [9, 14]), which is a non-linear, first-order differential equation.

The thesis is organized as follows. In chapter 2, the underlying principles and governing equations are derived. The methods of optimization used for achieving the goal of this thesis are introduced in chapter 3. In chapter 4 on ABH with rigid wall termination, it is shown how the optimization works and in chapter 5 the sound absorption in ABH with use of a porous material is studied. The achieved results of this thesis are summarized in chapter 6.

Chapter 2

Theory

This chapter is focused on the governing equations. First, a wave equation for acoustic pressure is derived in section 2.1, and from its solution restrictions for rectangular waveguide are obtained in section 2.2. In section 2.3, a generalized Webster equation for rectangular waveguides with varying both cross-section and wall impedance is derived. In section 2.4, the ABH geometry is introduced and in section 2.5, the black hole effect is shown. From the generalized Webster equation, a Riccati equation for reflection coefficient is derived in section 2.6. Finally, the porous material is employed in the ABH model in section 2.8 by a porous material inserted at the closed end of the ABH.

2.1 Wave equation for acoustic pressure

The wave equation for acoustic pressure can be derived based on a system of three equations describing fluid dynamics. First of them is Euler's equation for an ideal fluid

$$\rho \left[\frac{\partial \boldsymbol{v}}{\partial t} + (\boldsymbol{v} \cdot \boldsymbol{\nabla}) \boldsymbol{v} \right] = -\boldsymbol{\nabla} p \, , \tag{2.1}$$

where the left side is density ρ times acceleration $\mathrm{D}\boldsymbol{v}/\mathrm{D}t$ [1], and the right side is a negative pressure gradient $-\boldsymbol{\nabla} p$, meaning that the acceleration takes place in the direction of decreasing pressure.

The second of them is the equation for the conservation of mass in a fluid, also known as the continuity equation,

$$\frac{\partial \rho}{\partial t} + \boldsymbol{\nabla} \cdot (\rho \boldsymbol{v}) = 0 \, , \tag{2.2}$$

which expresses that the time rate of change of mass $\partial \rho / \partial t$ is equal to the net mass flux.

For the purposes of basic orientation, we would not consider the complete energy equation (see [10]) and instead focus only on state equation in thermally non-conducting and inviscid gas

$$\frac{p}{p_0} = \left(\frac{\rho}{\rho_0} \right)^{\gamma} \, , \tag{2.3}$$

[1] Here we abbreviate the operator $\partial/\partial t + \boldsymbol{v} \cdot \boldsymbol{\nabla}$ as $\mathrm{D}/\mathrm{D}t$, so $\partial \boldsymbol{v}/\partial t + (\boldsymbol{v} \cdot \boldsymbol{\nabla}) \boldsymbol{v} = \mathrm{D}\boldsymbol{v}/\mathrm{D}t$.

where p, p_0, ρ, ρ_0, γ are pressure, ambient pressure, fluid density, ambient fluid density and adiabatic exponent, respectively.

These introduced variables $\boldsymbol{v}, \rho$ and p are a sum of values in ambient state $\boldsymbol{v}_0, \rho_0, p_0$ (in absence of perturbations) and the acoustic disturbances $\boldsymbol{v}', \rho', p'$:

$$\boldsymbol{v}(\boldsymbol{x},t) = \boldsymbol{v}_0(\boldsymbol{x}) + \boldsymbol{v}'(\boldsymbol{x},t) \,, \tag{2.4}$$

$$\rho(\boldsymbol{x},t) = \rho_0 + \rho'(\boldsymbol{x},t) \,, \tag{2.5}$$

$$p(\boldsymbol{x},t) = p_0 + p'(\boldsymbol{x},t) \,. \tag{2.6}$$

We substitute these expressions into the set of equations considering only stagnant fluid (i.e., $\boldsymbol{v}_0 = \boldsymbol{0}$):

$$(\rho_0 + \rho') \left[\frac{\partial \boldsymbol{v}'}{\partial t} + (\boldsymbol{v}' \cdot \boldsymbol{\nabla}) \boldsymbol{v}' \right] = -\boldsymbol{\nabla}(p_0 + p) \,, \tag{2.7}$$

$$\frac{\partial(\rho_0 + \rho')}{\partial t} + \boldsymbol{\nabla} \cdot [(\rho_0 + \rho')\boldsymbol{v}'] = 0 \,, \tag{2.8}$$

$$\frac{p_0 + p'}{p_0} = \left(\frac{\rho_0 + \rho'}{\rho_0} \right)^{\gamma} \,. \tag{2.9}$$

In acoustics, the perturbances to an equilibrium state are very small ($|\rho'/\rho_0| \ll 1$, $|p'/p_0| \ll 1$), therefore the non-linear terms can be neglected, and the linear approximation (also called the *acoustic approximation*) can be used.

The linearized set of equations takes the following form

$$\rho_0 \frac{\partial \boldsymbol{v}'}{\partial t} = -\boldsymbol{\nabla} p' \,, \tag{2.10}$$

$$\frac{\partial \rho'}{\partial t} + \rho_0 \boldsymbol{\nabla} \cdot \boldsymbol{v}' = 0 \,, \tag{2.11}$$

$$p' = c_0^2 \rho' \,, \tag{2.12}$$

where c_0 is the adiabatic sound speed.

To derive the wave equation, we substitute the acoustic density $\rho' = p'/c_0^2$ from the linearized state equation (2.12) into the linearized continuity equation (2.11) in order to obtain:

$$\frac{1}{c_0^2} \frac{\partial p'}{\partial t} = -\rho_0 \boldsymbol{\nabla} \cdot \boldsymbol{v}' \,, \tag{2.13}$$

which is differentiated w.r.t. time:

$$\frac{1}{c_0^2} \frac{\partial^2 p'}{\partial t^2} = -\rho_0 \boldsymbol{\nabla} \cdot \frac{\partial \boldsymbol{v}'}{\partial t} \,. \tag{2.14}$$

We substitute $\partial \boldsymbol{v}'/\partial t$ from Euler's linearized equation, and this step finally yields the wave equation for acoustic pressure:

$$\nabla^2 p' = \frac{1}{c_0^2} \frac{\partial^2 p'}{\partial t^2} \,. \tag{2.15}$$

2.2 Wave propagation in a rectangular waveguide

The general solution of eq. (2.15) for wave propagation in a rectangular waveguide (shown in Figure 2.1) with rigid walls is obtained after employing the method of separation of variables (see [10]):

$$p' = \sum_{m=0}^{\infty}\sum_{n=0}^{\infty} p'_{mn} \,, \tag{2.16}$$

$$p'_{mn} = A_{mn}\cos\left(\frac{m\pi x}{a}\right)\cos\left(\frac{n\pi y}{b}\right)\exp(\mathrm{j}\omega t - \mathrm{j}k_{mn}z) \,, \tag{2.17}$$

where $\omega = 2\pi f$ is the angular frequency and

$$\left(\frac{m\pi}{a}\right)^2 + \left(\frac{n\pi}{b}\right)^2 + k_{mn}^2 = \left(\frac{\omega}{c_0}\right)^2 . \tag{2.18}$$

The equation (2.18) can be expressed in terms of the wave number k_{mn}:

$$k_{mn} = \sqrt{\left(\frac{\omega}{c_0}\right)^2 - \left(\frac{m\pi}{a}\right)^2 - \left(\frac{n\pi}{b}\right)^2} \,. \tag{2.19}$$

If $k_{mn} \in \mathbb{C}$, the wave is evanescent. In order for the specific mode m, n to propagate, the condition $k_{mn} \in \mathbb{R}$ must apply, i.e.

$$\frac{\omega^2}{c_0^2} - \left(\frac{m\pi}{a}\right)^2 - \left(\frac{n\pi}{b}\right)^2 \geq 0 \,, \tag{2.20}$$

or

$$\omega \geq c_0\sqrt{\left(\frac{m\pi}{a}\right)^2 + \left(\frac{n\pi}{b}\right)^2} \,. \tag{2.21}$$

This means that the lowest frequency, from which the specific mode m, n is able to propagate, is

$$\omega_{mn} = c_0\sqrt{\left(\frac{m\pi}{a}\right)^2 + \left(\frac{n\pi}{b}\right)^2} \,, \tag{2.22}$$

or

$$f_{mn} = \frac{c_0}{2\pi}\sqrt{\left(\frac{m\pi}{a}\right)^2 + \left(\frac{n\pi}{b}\right)^2} \,. \tag{2.23}$$

The mathematical model governing our rectangular ABH only describes the behaviour of quasi-plane waves. Thus it will be useful to derive the conditions under which the quasi-plane wave approximation can be used, i.e., how is defined the lowest frequency, where the first non-planar mode starts propagating through the waveguide.

If $a \geq b$, the first non-planar mode is $m = 1, n = 0$, it holds that

$$f_{1,0} \equiv f_{\mathrm{cut}} = \frac{c_0}{2\pi}\sqrt{\left(\frac{\pi}{a}\right)^2} = \frac{c_0}{2a} \,. \tag{2.24}$$

In order to use the quasi-plane wave approximation, we have to accommodate these restrictions: firstly, the frequency f of travelling wave should be lower than the cut-off frequency f_{cut} and secondly, $b \leq a$, where a, b are the waveguide height and width, respectively.

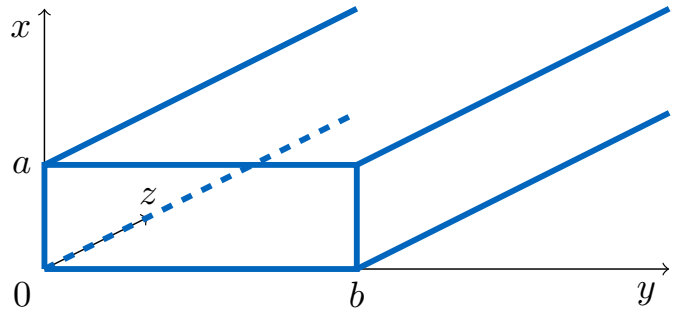

Figure 2.1: Rectangular waveguide

2.3 Rectangular waveguides with varying cross-section

While in the previous section, a rectangular waveguide with a constant cross-section was considered, in this section, a more general case will be derived. Now we consider a rectangular waveguide with a slowly varying cross-section $S = S(x) = 2a(x)b$ (see Figure 2.2). Moreover, we do not assume perfectly rigid walls. Instead, an admittance function $Y_w = Y_w(x)$ is prescribed on the walls' surface.

The Webster equation is derived from the continuity equation, Euler's momentum equation and the state equation. In this case, the general continuity equation (2.8) can be reduced to quasi one-dimensional form given by [3]:

$$\frac{1}{\rho_0}\frac{\partial \rho'(x,t)}{\partial t} + \frac{v'_x(x,t)}{S(x)}\frac{\mathrm{d}S(x)}{\mathrm{d}x} + \frac{\partial v'_x(x,t)}{\partial x} + \frac{2b}{S}v'_y(x,t) = 0\ , \tag{2.25}$$

where ρ_0, $\rho'(x,t)$, $S(x) = 2a(x)b$, $v'_x(x,t)$, $v'_y(x,t)$ are ambient density, the acoustic density, the cross-section, the component of the acoustic velocity in the x-axis direction and in the y-axis direction, respectively.

The component of the acoustic velocity in the y-axis direction $v'_y(x,t)$ can be written as

$$v'_y(x,t) = Y_w(x)p'(x,t)\ . \tag{2.26}$$

We substitute the equation (2.26) and the state equation $p'(x,t) = c_0^2\rho'(x,t)$ differentiated w.r.t. time into eq. (2.25) in order to get

$$\frac{1}{\rho_0 c_0^2}\frac{\partial p'(x,t)}{\partial t} + v'_x(x,t)\frac{1}{S(x)}\frac{\mathrm{d}S(x)}{\mathrm{d}x} + \frac{\partial v'_x(x,t)}{\partial x} + \frac{2b}{S}Y_w(x)p'(x,t) = 0\ . \tag{2.27}$$

This equation is then differentiated w.r.t. time and using the one-dimensional Euler's momentum equation

$$\frac{\partial v'_x(x,t)}{\partial t} = -\frac{1}{\rho_0}\frac{\partial p'(x,t)}{\partial x}\ , \tag{2.28}$$

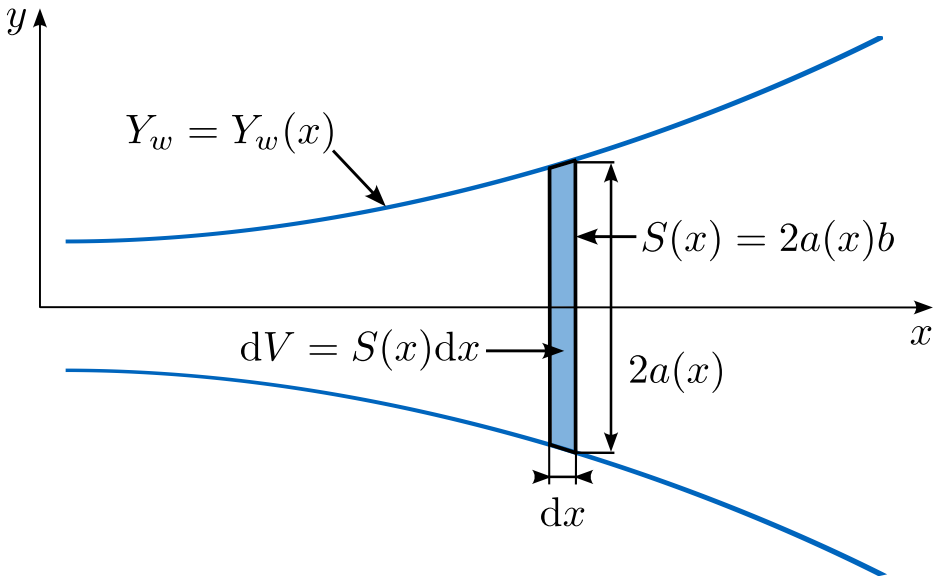

Figure 2.2: Schematic picture for the derivation of the generalized Webster equation.

the acoustic velocity $v'_x(x,t)$ is eliminated:

$$\frac{1}{\rho_0 c_0^2}\frac{\partial^2 p'(x,t)}{\partial t^2} - \frac{1}{\rho_0}\frac{1}{S(x)}\frac{\mathrm{d}S(x)}{\mathrm{d}x}\frac{\partial p'(x,t)}{\partial x} - \frac{1}{\rho_0}\frac{\partial^2 p'(x,t)}{\partial x^2} + \frac{2b}{S}Y_w(x)\frac{\partial p'(x,t)}{\partial t} = 0\,. \quad (2.29)$$

Since we consider the time-harmonic dependency of an acoustic field, the acoustic pressure is given by $p'(x,t) = \mathrm{Re}[P(x)\exp(\mathrm{j}\omega t)]$ and thus, we can write the eq. (2.29) as

$$\frac{\mathrm{d}^2 P(x)}{\mathrm{d}x^2} + \frac{1}{S(x)}\frac{\mathrm{d}S(x)}{\mathrm{d}x}\frac{\mathrm{d}P(x)}{\mathrm{d}x} + \left(k_0^2 - \frac{\mathrm{j}\omega\rho_0 2b}{S(x)}Y_w(x)\right)P(x) = 0\,, \quad (2.30)$$

where $k_0 = \omega/c_0$ is the wavenumber and $\mathrm{j} = \sqrt{-1}$ is the imaginary unit. Substituting the inner cross-section $S(x) = 2a(x)b$, we finally get the generalized Webster equation

$$\frac{\mathrm{d}^2 P}{\mathrm{d}x^2} + \frac{1}{a}\frac{\mathrm{d}a}{\mathrm{d}x}\frac{\mathrm{d}P}{\mathrm{d}x} + \left(k_0^2 - \frac{\mathrm{j}\omega\rho_0}{a}Y_w\right)P = 0\,. \quad (2.31)$$

2.4 ABH configuration

Now we have the generalized Webster equation (2.31) governing the acoustic pressure in a waveguide with varying cross-section and wall admittance. To obtain the mathematical model describing the wave propagation in ABH, we only need to specify the wall admittance function; the governing equation (2.31) remains the same.

The considered rectangular ABH is of the length L and height $2A$ and thus, the cut-off frequency of the ABH is $f_{\mathrm{cut}} = c_0/(4A)$. The cross-section of ABH is $2A \times B$, where $B \leq 2A$ is supposed. The ABH geometry is depicted in Figure 2.3.

The ABH consists of rigid ribs with varying heights, separated by narrow slits. The heights of the ribs are given by function $\ell(x) = A - a(x)$, where $a(x)$ is the profile function. The spatial period of ribs is defined as

$$W = \frac{L}{N_s} \,, \tag{2.32}$$

where L, and N_s are the length of ABH and number of slits, respectively. The width of a slit is described as $w = \xi W$, where $\xi \in (0, 1)$ is the rib-width to slit ratio, and the rib width as $(1 - \xi)W$.

The varying wall admittance $Y_w = Y_w(x, \omega)$ is derived from the plane wave solution to the linearized Navier-Stokes equations (LNSE) in narrow slits. It reads

$$Y_w(x, \omega) = \frac{\mathrm{j}\xi}{\rho_\mathrm{s} c_\mathrm{s}} \tan\left(\frac{\omega}{c_\mathrm{s}}\ell\right) \,, \tag{2.33}$$

where $c_\mathrm{s} = c_\mathrm{s}(\omega, w)$, $\rho_\mathrm{s} = \rho_\mathrm{s}(\omega, w)$, are the effective sound speed and effective unperturbed material density in air-filled slits. Their values are given by Stinson's model [15] of thermo-viscous losses in the narrow slit geometry.

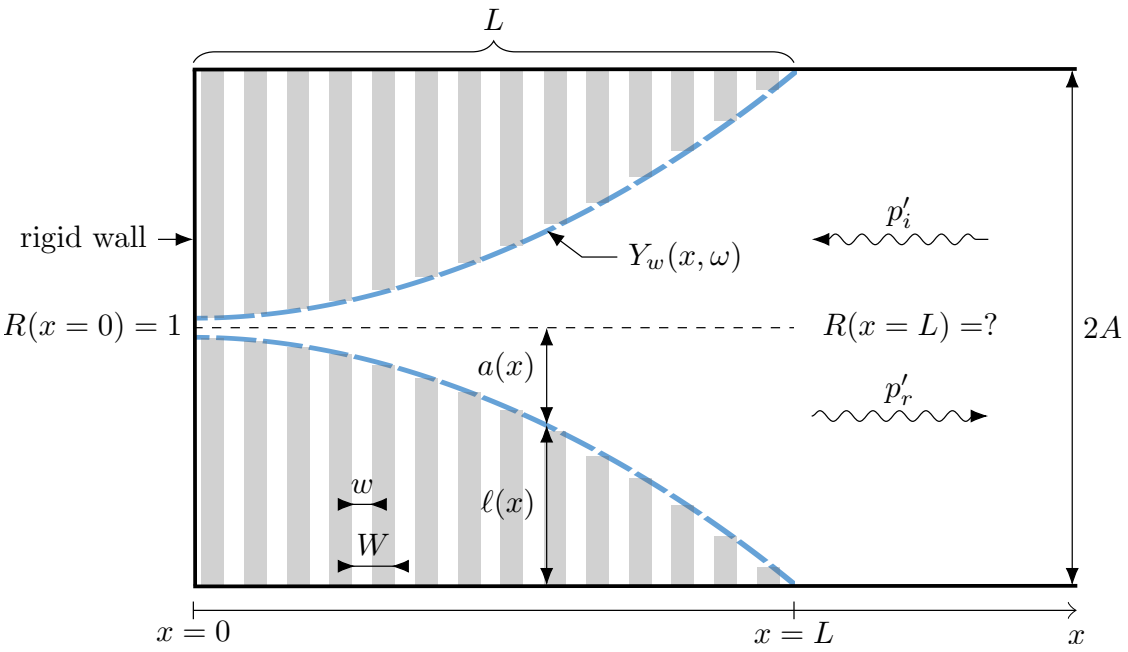

Figure 2.3: Profile diagram of the considered ABH

2.5 The Black hole effect

The idea of ABH was introduced by Mironov and Pislyakov [3]. The assumption was that due to the reduction of acoustic speed, the wave would never reach the end of the structure in finite time and thus, no wave would be reflected.

The black hole effect can be derived from the generalized Webster equation (2.31). To show it on a specific example, we consider a rectangular ABH with a quadratic profile function given by

$$a(x) = (-1)^n \frac{A}{L^n} x^n \,, \tag{2.34}$$

where $n = 2$ and a wall admittance approximation

$$Y_w(x, \omega) = \frac{\mathrm{j}k_0}{\rho_0 c_0}(A - a) \tag{2.35}$$

neglecting the influence of ribs thicknesses (i.e., considers infinitesimally narrow ribs) [12], the following equation is obtained:

$$\frac{\mathrm{d}^2 P}{\mathrm{d}x^2} + \frac{2}{x}\frac{\mathrm{d}P}{\mathrm{d}x} + \frac{k_0^2 L^2}{x^2} P = 0 \,. \tag{2.36}$$

A general solution for eq. (2.36) is given by

$$P(x) = C_+ \exp[\alpha_+ \ln x] + C_- \exp[\alpha_- \ln x] \,, \tag{2.37}$$

where $C_+, C_- \in \mathbb{R}$ are constants and

$$\alpha_\pm = \frac{1}{2}\left[-1 \pm \sqrt{1 - (2k_0 L)^2}\right] \,. \tag{2.38}$$

The local wavenumber $k(x)$ of a wave propagating towards the closed end is

$$k(x) = \frac{1}{2x}\sqrt{(2k_0 L)^2 - 1} \,, \tag{2.39}$$

see [12], and therefore, the group velocity of a wavepacket entering the ABH at $x = L$ is

$$c_g = \left(\frac{\partial k}{\partial \omega}\right)^{-1} = x \frac{c_0^2}{2L^2 \omega}\sqrt{(2k_0 L)^2 - 1} \,. \tag{2.40}$$

As the wavepacket approaches the closed end (as $x \to 0$), the group velocity tends to zero, and the time T needed for the wavepacket to reach the closed end of ABH tends to infinity, $T \to \infty$. This means following, the wave that entered the ABH would never reach the closed end leading to zero-reflection termination.

2.6 From generalized Webster equation to Riccati equation

As we are mainly concerned with reflection and absorption inside the ABH, it is useful to employ an equation written directly in terms of reflection coefficient R. Moreover, it is known that a whole class of wave equations for acoustic pressure with spatial inhomogeneity can be transformed into the Riccati equation (see e.g. [9, 14]), which is a first-order ordinary differential equation with one boundary condition.

The first step of the transform is done by replacing acoustic pressure with acoustic impedance $Z = Z(x, \omega)$ through relations derived from the linearized Euler's equation [2]

$$Z(x,\omega) = \frac{P(x,\omega)}{V_x(x,\omega)} = \frac{\mathrm{j}\omega\rho_0 P(x,\omega)}{\frac{\mathrm{d}P(x,\omega)}{\mathrm{d}x}} \tag{2.41}$$

$$\frac{\mathrm{d}P(x,\omega)}{\mathrm{d}x} = \frac{\mathrm{j}\omega\rho_0 P(x,\omega)}{Z(x,\omega)} \,. \tag{2.42}$$

After substitution, we get the Riccati equation for acoustic impedance

$$\frac{\mathrm{d}Z}{\mathrm{d}x} = \mathrm{j}\omega\rho_0 + \frac{1}{a}\frac{\mathrm{d}a}{\mathrm{d}x}Z - \left(\frac{\mathrm{j}\omega}{\rho_0 c_0^2} + \frac{Y_w}{a}\right) Z^2 \,. \tag{2.43}$$

Note that for acoustic impedance Z, it holds $Z = 0$ on a pressure-release surface and $Z = \infty$ on a rigid wall, i.e., the boundary condition of the differential equation at the closed end of ABH would be $Z = \infty$. Therefore, it is more convenient to have a model of ABH written in terms of reflection coefficient $R = R(x, \omega)$, which is easier to interpret and imagine, rather than in terms of acoustic impedance $Z = Z(x, \omega)$. For the reflection coefficient R, it holds $R = 0$ on a pressure-release surface and $R = 1$ on a rigid wall.

The reflection coefficient R and the acoustic impedance Z are related as follows

$$Z = \rho_0 c_0 \frac{1+R}{1-R} \,, \tag{2.44}$$

$$\frac{\mathrm{d}Z(x)}{\mathrm{d}x} = \frac{2\rho_0 c_0}{(1-R)^2}\frac{\mathrm{d}R}{\mathrm{d}x} \,. \tag{2.45}$$

We substitute the relations (2.44), (2.45) into equation (2.43) and, after some algebraic manipulation, we obtain

$$\frac{\mathrm{d}R}{\mathrm{d}x} = -\left(\frac{1}{2a}\frac{\mathrm{d}a}{\mathrm{d}x} + \frac{\rho_0 c_0 Y_w}{2a}\right) R^2 - \left(\mathrm{j}2k_0 + \frac{\rho_0 c_0 Y_w}{a}\right) R + \left(\frac{1}{2a}\frac{\mathrm{d}a}{\mathrm{d}x} - \frac{\rho_0 c_0 Y_w}{2a}\right) \,. \tag{2.46}$$

The solution of the eq. (2.46) must be obtained by a numerical method, preferably with an adaptive step, e.g., Runge–Kutta–Fehlberg method (RK45).

[2] Since we consider the time-harmonic dependency of an acoustic field, similarly as the acoustic pressure is given by $p'(x,t) = \mathrm{Re}[P(x)\exp(\mathrm{j}\omega t)]$, we can write the component of the acoustic velocity in the x-axis direction as $v'_x(x,t) = \mathrm{Re}[V_x(x)\exp(\mathrm{j}\omega t)]$.

2.7 The thermoviscous losses in the bulk of the ABH

However, this model equation (2.46) alone is not accurate (see Figure 2.4) because the thermoviscous losses in the bulk of the ABH are neglected. Thus, this model underestimates the damping properties of ABH. One way of solving this problem could be ad hoc to consider a complex sound speed $c = c_0(1 + \mu\mathrm{j})$, as it was suggested by Mironov [3]. However, this approach does not capture the underlying physics as it has been shown in [8]. As can be seen from Figure 2.4, in this case, it highly overestimates the damping.

Similarly, as for the thermoviscous losses in the slits between the ribs, the thermoviscous losses in the bulk of the ABH can be calculated employing Stinson's model [15]. Therefore, in eq. (2.43) the ambient fluid density ρ_0 and sound speed c_0 will be replaced by effective fluid density ρ_c and effective sound speed c_c. Note, that $\rho_c, c_c \in \mathbb{C}$. The eq. (2.43) will then take the form

$$\frac{\mathrm{d}Z}{\mathrm{d}x} = \mathrm{j}\omega\rho_c + \frac{1}{a}\frac{\mathrm{d}a}{\mathrm{d}x}Z - \left(\frac{\mathrm{j}\omega}{\rho_c c_c^2} + \frac{Y_w}{a}\right)Z^2 \,. \tag{2.47}$$

After substituting eq. (2.44), eq. (2.45), and performing some algebraic manipulation, we obtain the Riccati equation for reflection coefficient with thermoviscous losses in the bulk of the ABH:

$$\begin{aligned}\frac{\mathrm{d}R}{\mathrm{d}x} = &\left(-\frac{1}{2a}\frac{\mathrm{d}a}{\mathrm{d}x} - \frac{\rho_0 c_0 Y_w}{2a} - \frac{\mathrm{j}\omega}{2c_c}\frac{\rho_0^2 c_0^2 - \rho_c^2 c_c^2}{\rho_0 c_0 \rho_c c_c}\right)R^2 \\ &- \left(+\mathrm{j}2k_0 + \frac{\rho_0 c_0 Y_w}{a} + \frac{\mathrm{j}\omega}{c_c}\frac{\rho_0^2 c_0^2 + \rho_c^2 c_c^2}{\rho_0 c_0 \rho_c c_c}\right)R \\ &+ \left(+\frac{1}{2a}\frac{\mathrm{d}a}{\mathrm{d}x} - \frac{\rho_0 c_0 Y_w}{2a} - \frac{\mathrm{j}\omega}{2c_c}\frac{\rho_0^2 c_0^2 - \rho_c^2 c_c^2}{\rho_0 c_0 \rho_c c_c}\right) \,.\end{aligned} \tag{2.48}$$

It can be seen in Figure 2.4 that the results of governing equation (2.48) are an approximation close enough to use them further, e.g., for profile optimization. In this work, the FEM simulations used for validation are conducted in Comsol Multiphysics 5.5 (both for LNSE simulations and pressure wave equation with effective media given by Stinson and for porous materials, by JCAL).

2.8 Rectangular ABH with use of a porous material

The absorption of ABH can be further improved by inserting a porous material. A porous material is composed of a solid skeleton containing pores filled with a fluid, air in our case. Since the typical pore size is smaller than the characteristic wavelength of the sound waves, the processes occurring at the micro-scale can be described at the macro-scale as an effective medium by the Johnson-Champoux-Allard-Lafarge (JCAL) model by two effective parameters, effective density ρ_p and bulk modulus K_p (see [16] for state-of-the-art summary).

According to the JCAL Model, the porous material is characterized by six parameters, namely the flow resistivity, σ, porosity, ϕ, tortuosity, α_∞, viscous and thermal characteristic lengths, Λ and Λ' respectively, and the static thermal permeability, κ_0'. From these six

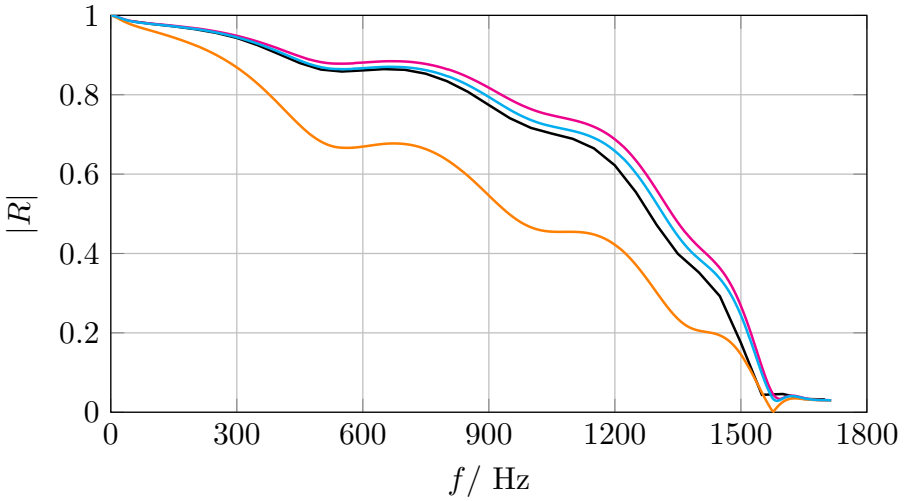

Figure 2.4: Comparison of models for reflection coefficient. Parameters of used ABH: $A = 0.05$ m, $L = 0.20$ m, $W = 2$ mm, $\xi = 0.5$, $f_{\text{cut}} = 1715$ Hz, linear profile. The black line (—) depicts the reflection coefficient spectra $|R|$ calculated employing LNSE in Comsol Multiphysics 5.5. The magenta line (—) depicts the result of equation (2.46) with no losses in the bulk of ABH. The orange line (—) is for equation (2.46) with losses according to Mironov [3] considering the complex sound speed $c = c_0(1 + 0.05\text{j})$. The blue line (—) depicts the result of equation (2.47) with losses in the bulk of ABH employing Stinson's effective parameters [15].

parameters, we obtain the aforementioned effective density ρ_p and bulk modulus K_p as

$$\rho_p(\omega) = \rho_0 \frac{\alpha_\infty}{\phi}\left[1 - \text{j}G_1(\omega)\sqrt{1 + \text{j}G_2(\omega)}\right], \tag{2.49}$$

$$K_p(\omega) = \frac{K_0}{\phi}\frac{1}{\gamma - (\gamma - 1)\left[1 - \text{j}G_1'(\omega)\sqrt{1 + \text{j}G_2'(\omega)}\right]^{-1}}, \tag{2.50}$$

where γ is the adiabatic exponent, $K_0 = \gamma P_0$ is the adiabatic bulk modulus and the functions $G_1(\omega), G_2(\omega), G_1'(\omega), G_2'(\omega)$ are given by

$$G_1(\omega) = \frac{\sigma\phi}{\alpha_\infty \rho_0 \omega}, \qquad G_2(\omega) = \frac{4\alpha_\infty^2 \rho_0 \eta \omega}{\sigma^2 \phi^2 \Lambda^2}, \tag{2.51}$$

$$G_1'(\omega) = \frac{\phi\eta}{\rho_0 \text{Pr} k_0' \omega}, \qquad G_2'(\omega) = \frac{4\text{Pr}\rho_0 k_0'^2 \omega}{\eta \phi^2 \Lambda'^2}. \tag{2.52}$$

For the following sections, it is convenient to define the effective wavenumber k_p and the characteristic acoustic impedance Z_p:

$$k_p = \frac{\omega}{c_p} = \omega\sqrt{\frac{\rho_p}{K_p}}, \tag{2.53}$$

$$Z_p = \sqrt{\rho_p K_p}, \tag{2.54}$$

where c_p is the effective sound speed in the porous material.

If we want to combine the effects of the ABH and porous material, there are multiple possible ways of implementation. For the purposes of this work, two ways of inserting the porous material were chosen: at the closed end of ABH (between the last pair of lamellas and the rigid wall, see subsection 2.8.1) and in the slits (see subsection 2.8.2).

2.8.1 Termination by a porous material

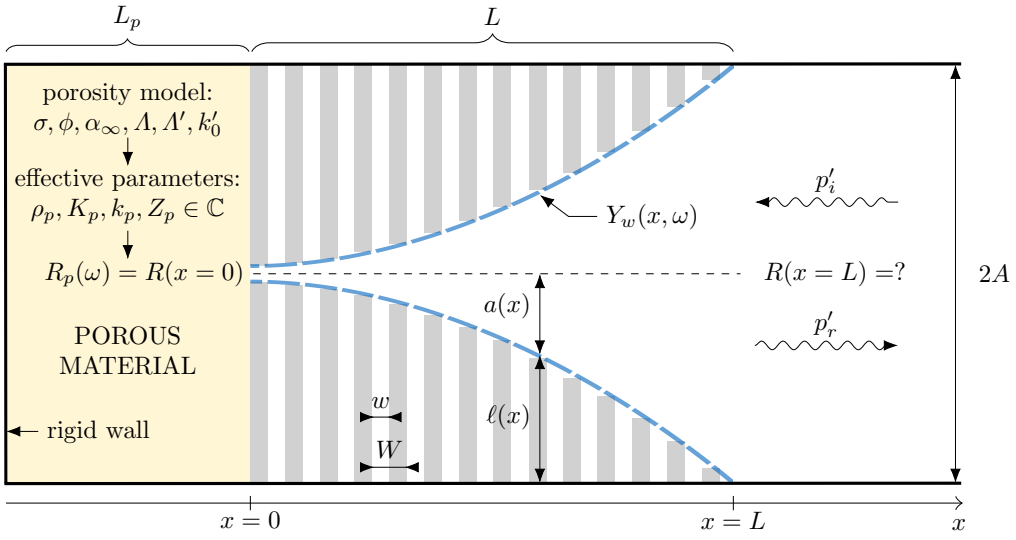

Figure 2.5: Profile diagram of the considered ABH terminated by a porous material

This chosen configuration, i.e., insertion of porous material at the closed end of ABH (as depicted in Figure 2.5), is very convenient for two reasons. Firstly, there is an advantage in terms of the practical feasibility: the porous material can be modelled as an effective medium almost without any condition affecting the geometry of the ABH, namely the width of slits. Secondly, the governing equation (2.48) remains the same; only the boundary condition $R(x = 0) = 1$ is replaced by reflection coefficient R_p, which is, for a given material, only frequency dependent.

Assuming only longitudinal plane waves $p'(x, t) = P(x) \exp(\mathrm{j}\omega t)$, the porous layer at the closed end of ABH can be modelled by the total transfer matrix (TMM, see [16])

$$\mathbf{T}_p = \begin{bmatrix} T_{11} & T_{12} \\ T_{21} & T_{22} \end{bmatrix} = \begin{bmatrix} \cos(k_p L_p) & \mathrm{j} Z_p \sin(k_p L_p) \\ \mathrm{j} \frac{1}{Z_p} \sin(k_p L_p) & \cos(k_p L_p) \end{bmatrix} . \tag{2.55}$$

The reflection coefficient for rigidly backed porous material is then

$$R_p = \frac{T_{11} - T_{21} Z_0}{T_{11} + T_{21} Z_0} , \tag{2.56}$$

where $R_p(\omega) \in \mathbb{C}$.

2.8.2 Porous material in slits

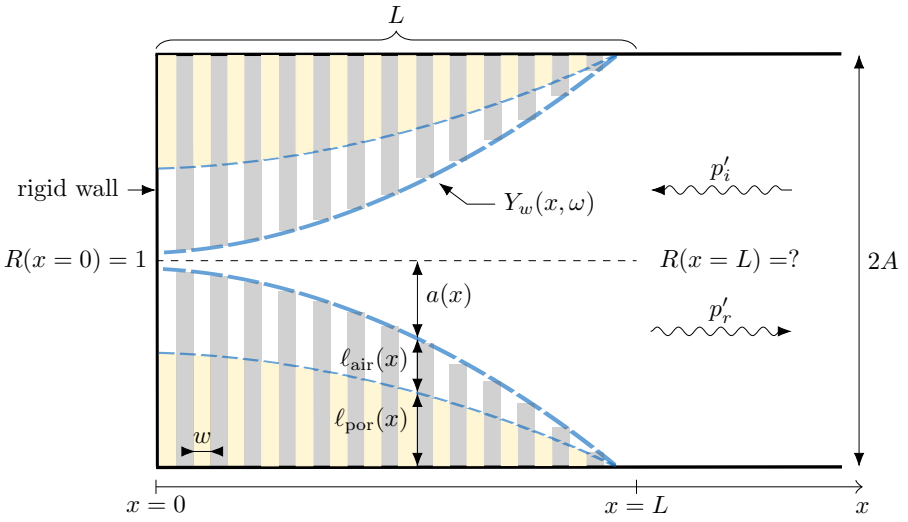

Figure 2.6: Profile diagram of the considered ABH employing slits filled with porous material (depicted in yellow).

Another possibility is to insert the porous material in the slits. In this case, we need to impose a condition for a minimum width of the slit, which needs to be sufficiently larger than the pore size to use the macro-scale model. For configuration depicted in Figure 2.6, the governing equation (2.48) remains the same together with the boundary condition $R(x = 0) = 1$. The only difference is the wall admittance function Y_w.

The slit partially filled by a porous material can be modelled by a total transfer matrix $\mathbf{T}_{\mathrm{slit}}$ which is equal to the matrix product of two elements

$$\mathbf{T}_{\mathrm{slit}} = \mathbf{T}_{\mathrm{air}}\mathbf{T}_{\mathrm{por}} \ , \tag{2.57}$$

where $\mathbf{T}_{\mathrm{air}}$, $\mathbf{T}_{\mathrm{por}}$ are the transfer matrices for the air and porous layer in the slit, respectively.

Then, with the use of eq. (2.44) and eq. (2.56), after some algebraic manipulation, we finally obtain the wall admittance as

$$Y_w = \frac{Z_{\mathrm{air}}\cos(k_{\mathrm{air}}\ell_{\mathrm{air}})\sin(k_{\mathrm{por}}\ell_{\mathrm{por}}) - Z_{\mathrm{por}}\cos(k_{\mathrm{por}}\ell_{\mathrm{por}})\sin(k_{\mathrm{air}}\ell_{\mathrm{air}})}{\mathrm{j}Z_{\mathrm{air}}Z_{\mathrm{por}}\cos(k_{\mathrm{air}}\ell_{\mathrm{air}})\cos(k_{\mathrm{por}}\ell_{\mathrm{por}}) + \mathrm{j}\sin(k_{\mathrm{air}}\ell_{\mathrm{air}})\sin(k_{\mathrm{por}}\ell_{\mathrm{por}})} \ , \tag{2.58}$$

where $\ell_{\mathrm{air}} = \ell_{\mathrm{air}}(x)$, $\ell_{\mathrm{por}} = \ell_{\mathrm{por}}(x)$ are depicted in Figure 2.6; k_{air}, k_{por}, Z_{air}, Z_{por} are the effective wavenumber for air given by Stinson's model [15] and for porous material given by JCAL Model [16], characteristic acoustic impedance for air and porous material, respectively.

Chapter 3

Methods

Firstly, in section 3.1, the main goal of optimization is described, and how it can be viewed in terms of setting the criterion for optimization. The wide range of possibilities for the subject of optimization is presented in section 3.2 together with our choice. Finally, the optimization algorithm itself is explained in section 3.3.

3.1 Goal of optimization

Our goal is to optimize the sound absorption in rectangular acoustic black holes, namely to minimize the reflection coefficient at the open end of ABH, i.e., $R(x = L)$, see Figure 2.3, 2.5. A possible alternative is to maximize the absorption coefficient of the rigidly-backed system at the open end of ABH, given by relation $\alpha = 1 - |R|^2$, i.e., maximize $\alpha(x = L)$.

Because both the reflection and absorption coefficients are frequency dependent, i.e., $R(x = L) = R(x = L, \omega)$ and $\alpha(x = L) = \alpha(x = L, \omega)$, we decided to minimize the surface area under the reflection coefficient curve, see Figure 3.1a, or alternatively, maximize the surface area under the absorption coefficient curve, see Figure 3.1b. Note that in order to maintain the minimization framework, instead of maximizing sound absorption α, from now on, negative absorption $-\alpha = R^2 - 1$ will be minimized.

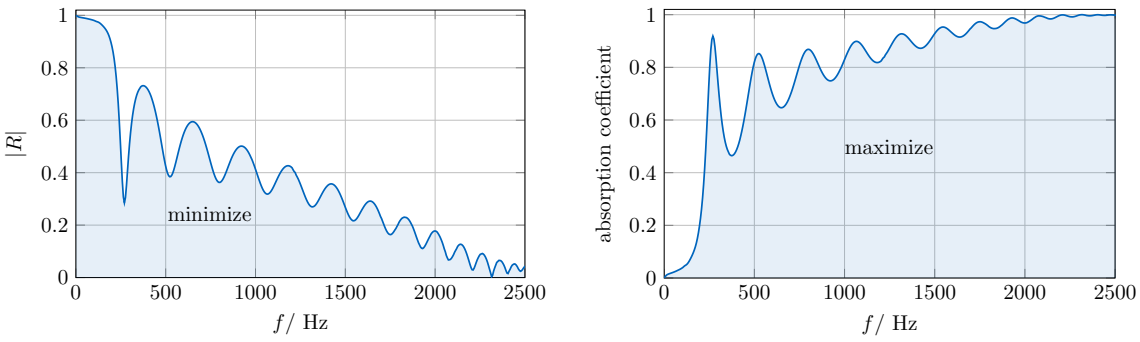

(a) (b)

Figure 3.1: (a) Reflection coefficient spectrum of ABH, (b) absorption coefficient of ABH

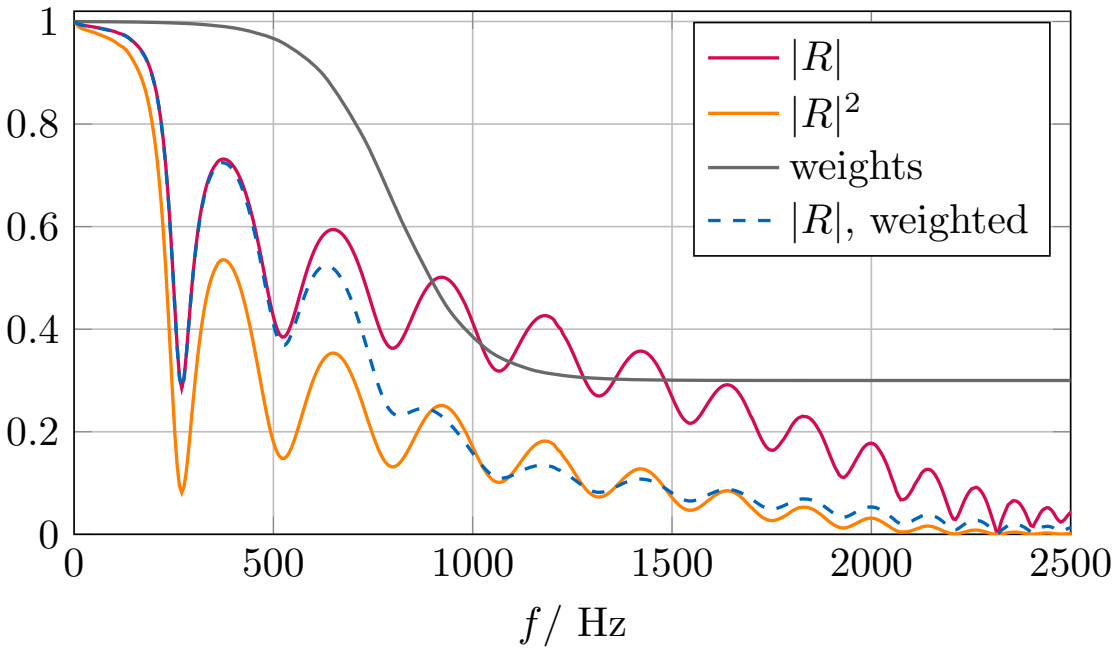

Figure 3.2: A graph for comparison of reflection coefficient, square root of reflection coefficient and weighted reflection coefficient

Eventually, the reflection coefficient R can be weighted, e.g. by a logistic function, and thus, desired frequency band can be emphasized, see Figure 3.2. A general logistic function is given by

$$\sigma(x) = \frac{a}{1 + \mathrm{e}^{-b(x-x_0)}} , \tag{3.1}$$

where a, b, x_0 are the supremum, the slope and the inflection point of the function, respectively. This way, optimization of low-pass, high-pass or band-pass filters could be targeted.

There is a difference between optimizing the reflection and absorption coefficient, such that the square root R^2 in absorption coefficient suppresses the influence of lower values of reflection, which occur more at the higher frequencies, as can be seen in Figure 3.2. Because our goal is mainly to improve the behaviour at lower frequencies, the mentioned difference can be viewed as an advantage of the cost function written in terms of absorption coefficient α. It offers us weighting-like properties with the benefit of being able to interpret the result of weighting the reflection coefficient R.

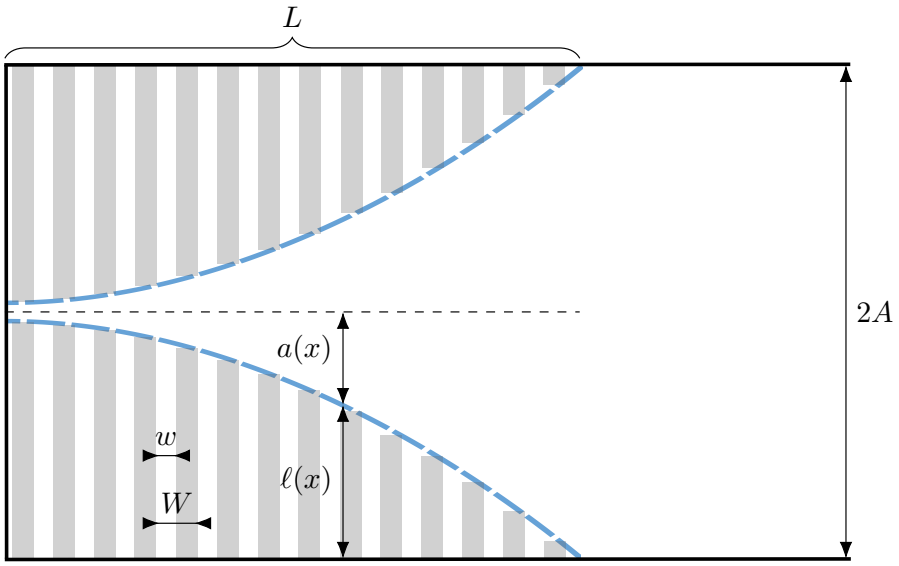

Figure 3.3: Possible parameters for optimization

3.2 Subject of optimization

The resulting coefficient, either reflection or absorption, is influenced by many parameters. However, not all of them are suitable to be the subject of optimization, therefore, it is essential to give an explanation of our choices.

A huge impact on the properties of ABH has the length L and height $2A$. Since the ABH is usually only a part of a device, these two parameters will be from now on considered as given parameters in order to fit in some geometry requirements. Note that it will be useful to work with a normalised ABH with length 1 and height $2A/L$. One of the reasons is the used profile function parametrisation, which will be discussed later in this section. This parametrisation is an advantage: the result of optimization could be applied to designing a device with different lengths L and heights $2A$ as long as the ratio A/L is kept.

The sound absorption is also affected by the width of the slit and rib. The optimization of these parameters can be implemented in many ways. It could be conveniently done by changing the spatial period W or the rib-width to slit ratio ratio ξ. Due to the practical feasibility, some requirements could be made, mainly on the minimum possible width of the slit. Potentially, as a subject of future work, both the spatial period W and the rib-width to slit ratio ratio ξ do not have to be constant; both can be a function of x. This approach could possibly better accommodate the differences between the absorption at lower and higher frequencies.

So far, the behaviour of ABHs with power-law profiles has been investigated. Though, optimizing the ribs-height function $\ell(x)$ offers the most possibilities (or eventually its complement, the profile function, $a = A - \ell$). In order to do that, it is useful to describe the ribs height function ℓ as a parametric curve and use the parameters as an input of the optimization.

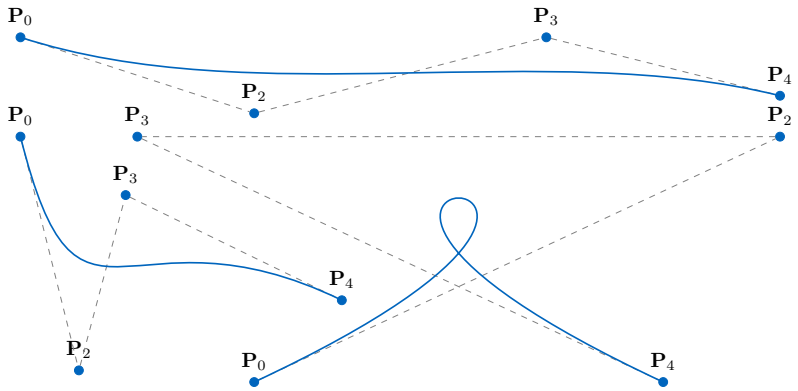

Figure 3.4: General Bézier curves

As was shown in section 2.5, the profile of ABH has to be a continuous, smooth, slowly varying curve. Due to these requirements, higher degree polynomial functions are unsuitable for this purpose, as they can change quite wildly even for small changes of coefficients of individual terms. For modelling smooth and continuous curves, a parameterization known as a Bézier curve is widely used.

In general, a Bézier curve of n-th order is defined for a set of $n+1$ control points $\mathbf{P}_0$, $\mathbf{P}_1$, $\mathbf{P}_2$, ..., $\mathbf{P}_n$ by

$$\mathbf{C}(u) = \sum_{i=0}^{n} \mathbf{P}_i B_{i,n}(u) \ , \tag{3.2}$$

where $u \in [0,1]$ and $B_{i,n}(u)$ is a Bernstein polynomial (sometimes called a Bézier basis function) given by

$$B_{i,n}(u) = \binom{n}{i} u^i (1-u)^{n-i} \ , \tag{3.3}$$

where $\binom{n}{i}$ is a binomial coefficient. The endpoints $\mathbf{P}_0$ and $\mathbf{P}_n$ are a part of the Bézier curve $\mathbf{C}(u)$, other control points lie on the curve only in specific cases. The line segments $\mathbf{P}_0\mathbf{P}_1$, $\mathbf{P}_1\mathbf{P}_2$, ..., $\mathbf{P}_{n-1}\mathbf{P}_n$ form together the so-called control polygon, see Figure 3.4.

The first caveat is that any change to a control point will influence the entire curve, hence it is not possible to make changes only on a local scope. The second one is the domain of the Bézier curve has to be $[0,1]$. Fortunately, this is not a problem in our case, since the domain of the ABH profile, after the aforementioned normalization, is already in $[0,1]$.

However, this approach to the parametric curve offers two main advantages. From the fact that a second-order Bézier curve is a segment of a parabola and thus a segment of a parabola can be described by the Bézier curve, it follows that the quadratic ribs-height function mentioned in related papers (such as [8]) can be used as a benchmark solution or an initial guess for the optimization. The second advantage is that any n-th order Bézier curve with control points $\mathbf{P}_0$,..., $\mathbf{P}_n$ is also a $(n+1)$-th Bézier curve with control points $\mathbf{P}'_0$,...,

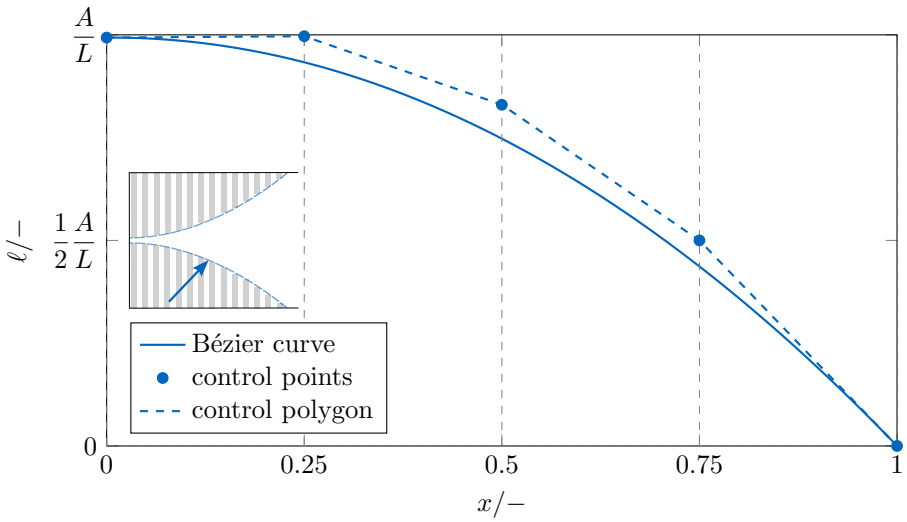

Figure 3.5: A Bézier curve adapted to the geometry of ABH

$\mathbf{P}'_{n+1}$. They are related by

$$\mathbf{P}'_i = \frac{i}{n+1}\mathbf{P}_{i-1} + \left(1 - \frac{i}{n+1}\right)\mathbf{P}_i \,, \quad i = 0,\ ..., n+1 \,, \tag{3.4}$$

where i denotes the i-th control point $\mathbf{P}_i$. This means a sub-optimal solution can be further optimized with more degrees of freedom.

For the purposes of describing the ribs-height function ℓ and its further use in optimization, some restrictions need to be adopted. In Figure 3.5, an example of a Bézier curve adapted to the geometry of ABH can be seen. Firstly, let the points $\mathbf{P}_i = (x_i, y_i)$ be equidistantly distributed along the x-axis and only the y-coordinate be variable. Secondly, let the endpoint $\mathbf{P}_n$ be fixed as $\mathbf{P}_n = (1, 0)$ because otherwise, it may cause unwanted impedance mismatch at the entry of ABH. Therefore, from now on, this point $\mathbf{P}_n$ will not be considered as a control point and thus will not be a subject of optimization.

Furthermore, in order to prevent the denominator, i.e., the profile function a, in governing equations Eq. 2.48 from being zero, which may cause unpredicted behaviour in the code, the following condition must always hold $\ell < A/L$. Therefore the y-coordinate of the endpoint $\mathbf{P}_0$ should be always in $[0, A/L)$. Because of computer precision, it is useful to specify a coefficient $\ell_{max} \in (0, 1)$ defining the maximum height of rib as $\ell_{max} A/L$.

However, this restriction is not enough, as it controls only the endpoint $\mathbf{P}_0$. It should also be guaranteed by the optimization algorithm that any of the ribs will not exceed the maximum height $\ell_{max} A/L$. There are two ways of controlling this condition: by evaluating the Bézier curve at finitely many points along the whole curve, which is computationally more demanding than defining a maximum value $\ell_{max} A/L$ for the control points. The second option can be ensured by the optimization algorithm itself by specifying boundaries for the subject of optimization.

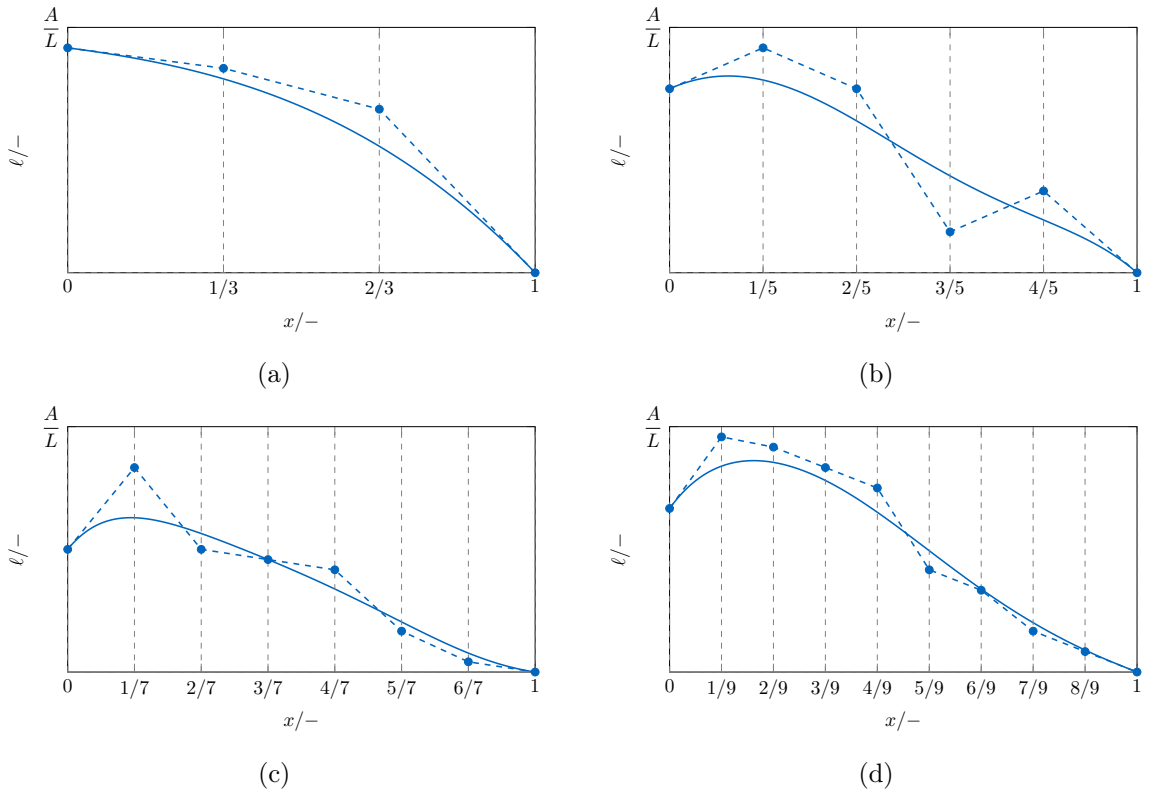

Figure 3.6: Examples of a (a) 3rd order, (b) 5th order, (c) 7th order, (d) 9th order Bézier curve variability, adapted to the geometry of ABH.

The optimal number of Bézier control points for our purposes is not known. It follows from our preliminary numerical experiments that a Bézier curve of less than the 3rd order does not offer enough variability. On the contrary, more than the 9th order can lead to so quickly varying profiles that the final real design would not correspond to the theoretical model. The examples of the Bézier curve variability can be seen in Figure 3.6.

3.3 Optimization algorithm

The problem with the optimization is that there is no clear relationship between the reflection coefficient curve and the subject of optimization itself, the ribs height function ℓ. It is only known that the lower frequency waves tend to travel to the closed end of ABH. The higher the frequency is, the closer to the open end the wave is absorbed, see [8]. Therefore it was decided to employ a derivative-free optimization.

This could be solved by an optimization algorithm called Evolution Strategies (ES), inspired by the theory of evolution in nature, mutation and selection [17]. The current state-of-the-art method is a particular type of ES, a Covariance Matrix Adaptation Evolution Strategy (CMA-ES), which is specifically designed for nonlinear non-convex black-box optimization [18].

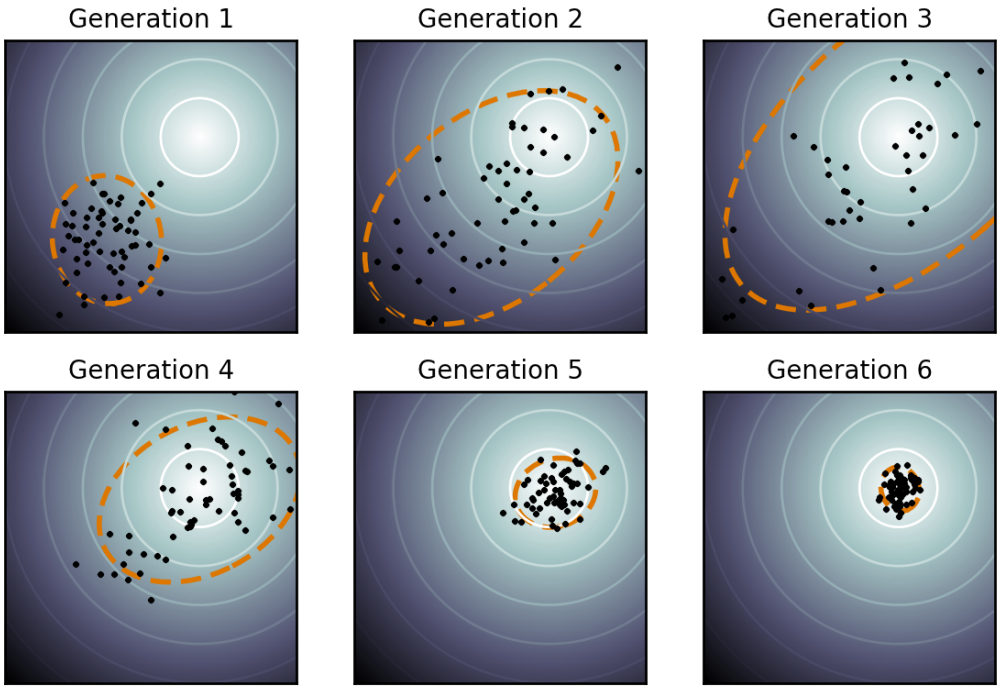

Figure 3.7: Illustration of CMA-ES process for a two-dimensional problem (from [19]). The black dots show the population, and the orange dashed line depicts the distribution of the population. The optimization landscape is depicted with solid lines of equal values, and the brightest spot signifies the global optimum. Within a few generations, the population is concentrated in the global optimum.

In CMA-ES, the parameters meant to be set by the user are the population size λ, initial solution $\boldsymbol{m}$ (the initial guess, i.e., in our case, the Bézier control points), the initial standard deviation σ (the step-size) and, eventually, the termination criteria. Note that the optimal solution should be in the initial solution hypercube given by $\boldsymbol{m} \pm 3\sigma(1, ..., 1)^\top$ [18] and that population size λ should be set accordingly to our goal. While a smaller population size leads to faster convergence and more local search behaviour, the larger λ offers a faster adaptation of the covariance matrix and more global search behaviour.

The search space dimension n is given by the number of Bézier control points to be optimized and possibly some additional parameters. An example of the CMA-ES in the two-dimensional search space is depicted in Figure 3.7.

After initialization, the CMA-ES is run in loops, called generations, until one of the termination criteria is met. In each generation, four main parts take place, as represented in pseudocode Algorithm 1. Firstly, a new population of λ samples is produced and evaluated. Then, the population is sorted according to the values of cost function f_i, and the mean $\boldsymbol{m}$ is updated as a weighted average of μ selected points with the lowest values of cost function. Next, based on the cumulative step-size adaptation, the step-size σ is updated. Finally, the covariance matrix is adapted to increase the likelihood of successful steps.

Algorithm 1 Covariance Matrix Adaptation Evolution Strategy (CMA-ES)

set the population size λ and generation $g = 0$
initialization:
    $\boldsymbol{m}^{(0)}$ distribution mean (initial guess)
    $\sigma^{(0)}$ initial step-size
    $\boldsymbol{C}^{(0)} = \mathbf{I}$ covariance matrix
    $\boldsymbol{p}_\sigma^{(0)} = \mathbf{0}$, $\boldsymbol{p}_\mathrm{c}^{(0)} = \mathbf{0}$ evolution paths
while termination criterion not met **do**
    sample new population and evaluate the offsprings:
        for i in $\{1, ..., \lambda\}$ **do**
            $\boldsymbol{x}_i^{(g+1)} \sim \boldsymbol{m}^{(g)} + \sigma^{(g)} \mathcal{N}(\mathbf{0}, \boldsymbol{C}^{(g)})$
            $f_i = \mathrm{cost\_function}(\boldsymbol{x}_i)$
    selection and recombination:
        $\boldsymbol{x}_{1:\lambda}^{(g+1)} \leftarrow \mathrm{sort\_solutions}(); \; f(\boldsymbol{x}_1) \leq ... \leq f(\boldsymbol{x}_\lambda)$
        $\boldsymbol{m}^{(g+1)} \leftarrow \mathrm{update\_mean}(\boldsymbol{x}_{1:\lambda})$
    step size control:
        $\boldsymbol{p}_\sigma^{(g+1)} \leftarrow \mathrm{update\_ps}(\boldsymbol{p}_\sigma^{(g)}, \; \boldsymbol{m}^{(g+1)} - \boldsymbol{m}^{(g)}, \; \sigma^{(g)}, \; \boldsymbol{C}^{(g)})$
        $\sigma^{(g+1)} \leftarrow \mathrm{update\_sigma}(\sigma^{(g)}, \; \boldsymbol{p}_\sigma^{(g+1)})$
    covariance matrix adaptation:
        $\boldsymbol{p}_\mathrm{c}^{(g+1)} \leftarrow \mathrm{update\_pc}(\boldsymbol{p}_\mathrm{c}^{(g)}, \; \boldsymbol{m}^{(g+1)} - \boldsymbol{m}^{(g)}, \; \sigma^{(g)})$
        $\boldsymbol{C}^{(g+1)} \leftarrow \mathrm{update\_cov}(\boldsymbol{C}^{(g)}, \; \boldsymbol{p}_\mathrm{c}^{(g+1)}, \; (\boldsymbol{x}_{1:\lambda}^{(g+1)} - \boldsymbol{m}^{(g)})/\sigma^{(g)})$
    $g \leftarrow g + 1$
return $\boldsymbol{x}_1$ or $\boldsymbol{m}$

The theoretical model of ABH, i.e., the governing equations and the parametrization of the ribs-height function ℓ, is written in Python using libraries NumPy [20] and SciPy [21]. The optimization algorithm for the purpose of optimizing sound absorption in rectangular ABHs was implemented using the open-source Python library for CMA Evolution Strategy [22].

Chapter 4

Optimization of ABH with rigid wall termination

The main purpose of this chapter is to show how the optimization works. Firstly, in section 4.1 the benchmarks will be introduced together with its properties. Then in section 4.3 and section 4.4, the different runs and settings of optimization will be described, and the results will be compared in section 4.5. Note, that we aim for practical feasibility and thus, throughout the whole chapter, only geometries that can be nowadays easily 3D printed are considered.

Throughout this text, we consider the following values of material quantities (air in our case): adiabatic sound speed $c_0 = 343\ \mathrm{m\,s^{-1}}$, air density $\rho_0 = 1.2\ \mathrm{kg\,m^{-3}}$, dynamic viscosity $\mu = 1.83 \times 10^{-5}\ \mathrm{Pa\,s}$, adiabatic exponent $\gamma = 1.4$, specific heat capacity at constant pressure $c_p = 1004\ \mathrm{J\,kg^{-1}\,K^{-1}}$, thermal conductivity $\varkappa = 2.59\ \mathrm{W\,m^{-1}\,K^{-1}}$ and the Prandtl number $\mathrm{Pr} = 0.71$. The adiabatic bulk modulus is given as $K_0 = \gamma P_0$, where $P_0 = \rho_0 c_0^2/\gamma$ is the static pressure.

4.1 Benchmarks and initial solutions

It is crucial to clarify the difference between the terms *benchmark* and *initial solution*. An ABH benchmark is defined by its ribs-height functions ℓ, its height-length ratio A/L, its spatial period of ribs W, and its rib-width to slit ratio ξ, see Figure 3.3. From now on, the reflection and absorption coefficient spectra of the benchmarks and optimized solutions will be compared. On the other hand, an initial solution is defined only by the Bézier control points, since those are the only parameters to be optimized.

Two specific benchmarks have been chosen. The chosen benchmarks are ABHs with a linear and quadratic ribs-height function ℓ, see Figure 4.1. The reason for this decision is that these two ribs-height functions are the current state-of-the-art [2], although almost entirely only for ABHs with circular cross-sections.

For the definition of initial ribs-height functions ℓ, we will use the quadratic profile function a given by

$$a = \frac{A}{L}\left[a_0 + (1 - a_0)x^2\right] , \tag{4.1}$$

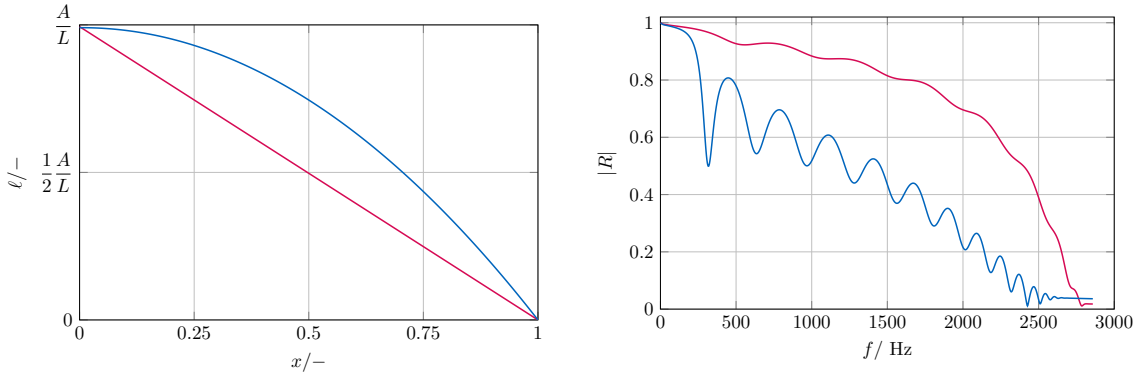

(a) (b)

Figure 4.1: Benchmarks. Illustration of (a) ribs-height function ℓ and (b) reflection coefficient spectrum $|R|$. The red line depicts the linear initial solution, the blue line depicts the quadratic initial solution. Figure (b) depicts the reflection coefficient spectra $|R|$ that we are trying to outperform in the optimization.

where A, L, a_0 are the half-height of ABH, the length of ABH, and the value used to control the profile of ABH at $x = 0$, respectively. After substituting the transformation $a = A/L - \ell$ and $a_0 = 1 - \ell_0$, we obtain

$$\ell = \frac{A}{L}\ell_0 \left(1 - x^n\right) \tag{4.2}$$

where $n = 1$ for the linear ribs-height function and $n = 2$ for the quadratic ribs-height function. In order to ensure the convergence of governing equations and avoiding division by zero, as was mentioned in section 3.2, the maximum height of ribs was set as $\ell_0 = 0.994$.

The benchmark parameters A, L, W and ξ will be chosen in order to guarantee the practical feasibility of 3D printing of the device, which is our aim. For the specification of parameters defining the ABH benchmark other than the ribs-height function ℓ, it is needed to discuss the aimed frequency band which is connected to the human auditory spectrum. The human audible range is said to be from 20 to 20 000 Hz [23]. Therefore, the lower boundary of the aimed frequency band is about 20 Hz.

The upper boundary of the aimed frequency band is defined by the cut-off frequency $f_{\text{cut}} = c_0/(4A)$. Above this frequency, the quasi-plane wave approximation is not valid and thus, it is not possible to use the governing equation (2.48), as was described in section 2.2.

Because our aim is the practical feasibility of the device, the ABH height $2A$ and length L are limited by the maximum print area size of a 3D printer, which is, in our case, 25 x 21 x 21 cm [24]. In order to have enough room for manipulation, it was decided to set the ABH half-height and length as $A = 0.03$ m, $L = 0.2$ m, respectively.

Similarly, for the spatial period of ribs W. As can be seen from the Figure 4.2, with decreasing W, the solution can always be improved. The ideal solution could be achieved with infinitely thin ribs, which is possible only in numerical simulations, not in real-world applications.

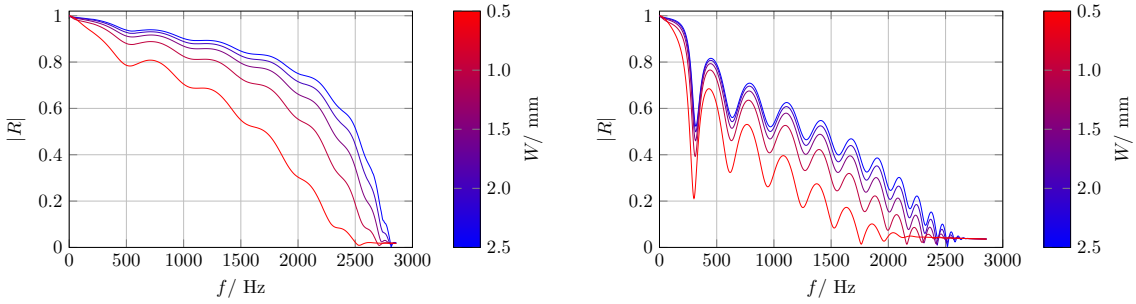

Figure 4.2: Reflection coefficient spectra $|R|$ for a (a) linear, (b) quadratic ABH with $W = \{1, 2, 3, 4, 5\}$ mm and fixed $\xi = 0.5$, $A_0 = 0.03$ m, $L = 0.2$ m.

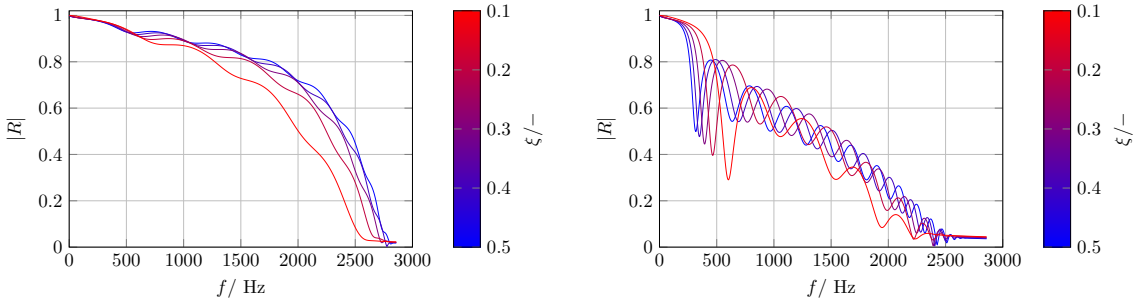

Figure 4.3: Reflection coefficient spectra $|R|$ for a (a) linear, (b) quadratic ABH with $\xi = \{0.1, 0.2, 0.3, 0.4, 0.5\}$ and fixed $W = 4$ mm, $A = 0.03$ m, $L = 0.2$ m.

The minimum possible rib width w is usually 1-2 mm. It depends on the application (e.g. on the level of stress in the material) and on the 3D printer nozzle diameter. The maximum of the rib width w is bounded by

$$w \ll \lambda_{\min} = \frac{c_0}{f_{\text{cut}}} = 4A \,, \tag{4.3}$$

so the sequence of the ribs behaves as a continuous wall from the point of view of the shortest wave propagating in the structure, as was justified in section 2.3. Our decision is to set the ribs' width as $w = 2$ mm and the spatial period of ribs as $W = 4$ mm.

The influence of the aspect ratio ξ can be seen in Figure 4.3. For simplicity, equally wide ribs and gaps will be considered, i.e. $\xi = 0.5$.

To conclude, our choice of parameters for the benchmarks are $A = 0.03$ m, $L = 0.2$ m, $W = 4$ mm and $\xi = 0.5$. This choice of parameters is quite illustrative, taking into account the aforementioned properties and the practical feasibility of the device. The optimization will be started with two different initial solutions. The first of them is the linear ribs-height function ℓ with $\ell_0 = 0.994$ and Bézier control points (0.14909, 0.074545), the second of them is the quadratic ribs-height function ℓ with $\ell_0 = 0.9905$ and Bézier control points (0.148575, 0.1492875).

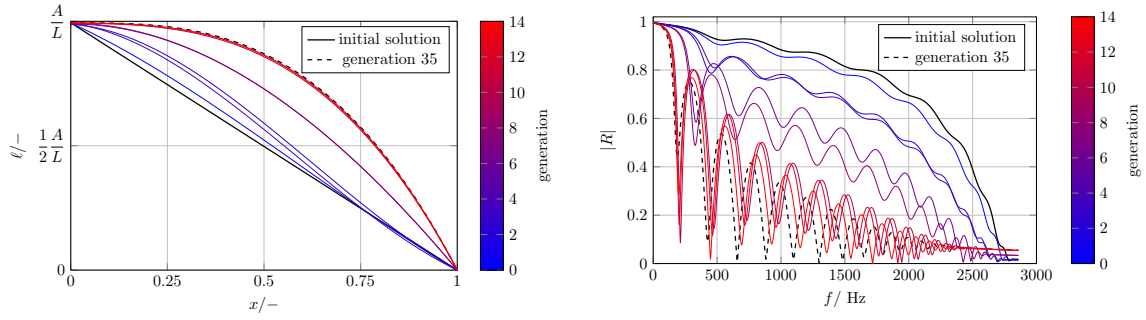

(a) (b)

Figure 4.4: Optimization progress with 3 control points: (a) ribs-height function ℓ, (b) reflection coefficient R

4.2 Cost function

The cost function for the optimization of ABH with rigid termination is proposed in the form of the minimization of the surface area under the reflection coefficient spectra as

$$\int_0^{f_{\text{cut}}} |R(f)| \mathrm{d}f \ . \tag{4.4}$$

However, the reflection coefficient spectrum is numerically evaluated using eq. (2.48) at finitely many frequencies f_i. The number of frequencies N defines how fine and smooth the reflection coefficient will be; it is a parameter to be set in dependency on both the accuracy we want to achieve and the computational time we are able to invest. The definite integral (4.4) is approximated by the trapezoidal rule.

4.3 ABH optimization with linear initial solution

The first chosen initial solution ribs-height function ℓ is a linear function given by eq. (4.2) with $\ell_0 = 0.994$ and Bézier control points (0.14909, 0.07455), see Figure 4.1a. The reflection coefficient is evaluated for frequencies $f \in \{f_1, ..., f_N\}$, where $N = 500$ is the number of evaluated frequencies, $f_1 = 1$ Hz and $f_N = f_{\text{cut}} = 2858$ Hz for the given geometry $A = 0.03$ m.

4.3.1 Run 1 with 3 control points

The first run with three initial solution control points (0.14909, 0.09940, 0.04970), $\lambda = 64$ and $\sigma = 0.01$, repeatedly ended up in local optimum with control points (0.14909, 0.14909, 0.14909), i.e., the upper boundaries $l_{max}A/L \cdot$ (1,1,1). The best offsprings for the first 14 generations of ribs-height function evolution can be seen in Figure 4.4a and, in corresponding colours, the evolution of reflection coefficient in Figure 4.4b. After generation 14, the speed of evolution slowed down and ended after generation 35.

4.3.2 Run 2 with 4 control points

We assume the ABH could perform better in terms of the reflection coefficient than in the previous run. As the first run of evolution converged to a local optimum on the boundary of the given interval, it was decided not to use this result and instead increase the number of control points by one. The initial solution for the second run is again the linear ribs-height function, given by four control points (0.14909, 0.111825, 0.07455, 0.037275).

The evolution ended after 36 generations; the best solution (0.14909, 0.14909, 0.14906, 0.11099) was achieved in generation 31, see Figure 4.5. Although the reflection coefficient curve of the best solution is very similar to the optimal result in subsection 4.3.1, one additional control point provided enough flexibility, and thus, the control points have not converged to the maximum value. Note that it was not due to a too early convergence, but because the achieved best solution is more favorable in terms of cost function than all four control points on their maximum value.

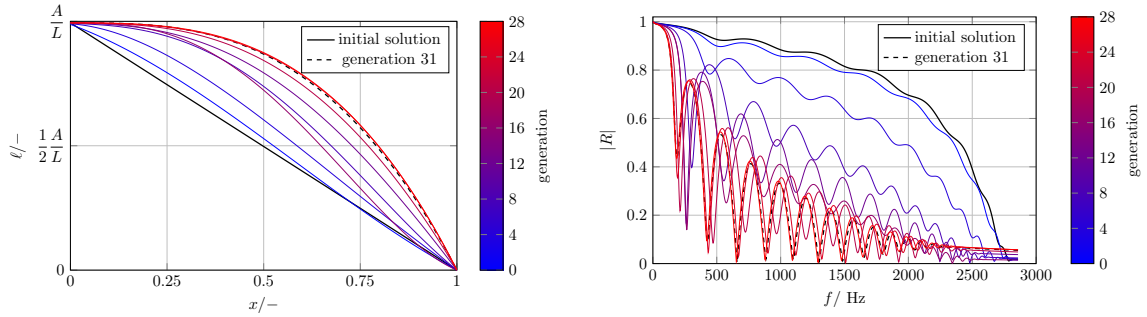

(a) (b)

Figure 4.5: Optimization progress with 4 control points: (a) ribs-height function ℓ, (b) reflection coefficient R

4.3.3 Run 3 with 5 control points

As the optimization with 4 control points was successful, and for further improvement more degrees of freedom are needed, the Bézier curve order of the best solution from subsection 4.3.2 will be elevated by one to get the initial solution (0.14909, 0.14909, 0.14907, 0.13383, 0.08879) for this run. In order to ensure slightly more local search than in the previous section, the step-size is reduced to $\sigma = 0.005$.

During the first 11 generations, the Bézier curve is only oscillating around the initial solution and the result was only getting worse, see Figure 4.6.

After generation 12, the reflection coefficient curve slowly began to improve. The best result was achieved in generation 38 with control points (0.14909, 0.14909, 0.14909, 0.14907, 0.02857).

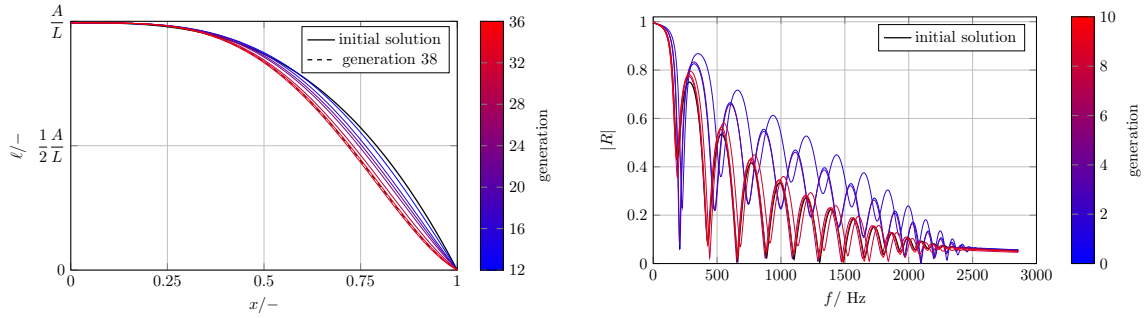

(a) (b)

Figure 4.6: Optimization progress with 5 control points for generations 0-10: (a) ribs-height function ℓ, (b) reflection coefficient R

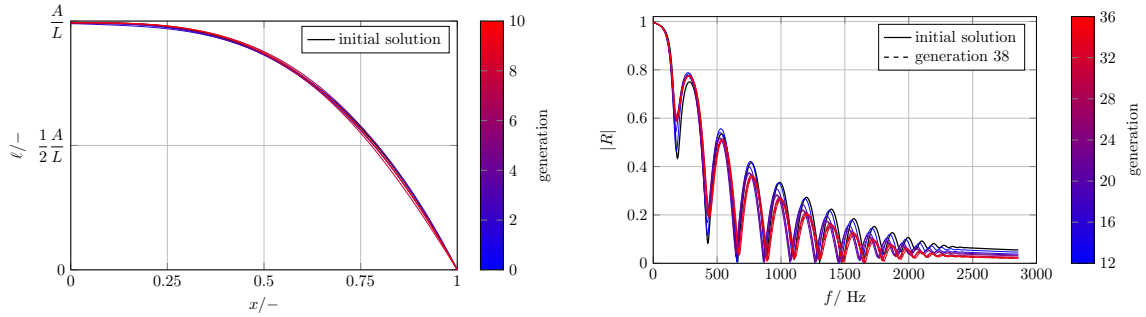

(a) (b)

Figure 4.7: Optimization progress with 5 control points for generations 12-38: (a) ribs-height function ℓ, (b) reflection coefficient R

4.3.4 Run 4 with 6 control points

The degree of the Bézier curve describing best ribs-height function ℓ was again elevated to get the initial solution (0.14909, 0.14909, 0.14909, 0.14908, 0.1089, 0.02381) for a new run, the step-size remained the same $\sigma = 0.005$. It was found that in this situation with this setting the solution cannot be improved. For the first 35 generations, the reflection coefficient was much worse than the initial guess and for the next 9 generations, the solution just oscillated around the initial guess. The optimum (0.14909, 0.14909, 0.14907, 0.14897, 0.10545, 0.02874) was achieved in generation 44. However, it is only insignificantly better than the initial guess, therefore it was decided the result of this run will not be used further.

4.3.5 Run 5 with 7 control points

Since the last run did not lead to any improvement, the initial solution from subsection 4.3.4 will be reused with one more control point. The initial guess for this run is then (0.14909, 0.14909, 0.14909, 0.14908, 0.13186, 0.08459, 0.02041), the population size λ remains the same and the step-size is reduced to $\sigma = 0.002$.

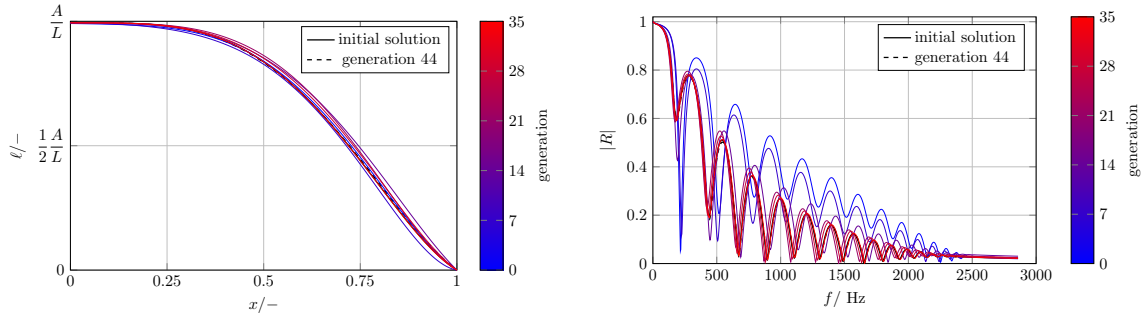

(a) (b)

Figure 4.8: Optimization progress with 6 control points: (a) ribs-height function ℓ, (b) reflection coefficient R

In order to target the lower frequencies, it was decided to use the weighting of the cost function (4.4). The weights were chosen as

$$weights = 0.5 + \frac{0.5}{1 + \mathrm{e}^{0.03\cdot(\{f\}-600)}} \ , \tag{4.5}$$

where $\{f\}$ are the numerical values of frequencies for which the reflection coefficient R is evaluated. The weights and their influence on the reflection coefficient curve can be seen in Figure 4.9.

The reflection coefficient began to improve after generation 21 of this run and the optimal solution (0.14909, 0.14909, 0.14905, 0.14895, 0.14907, 0.04900, 0.04766) was reached in generation 45. This result ensures a smaller surface under the reflection coefficient curve than the result in subsection 4.3.3 with only five control points.

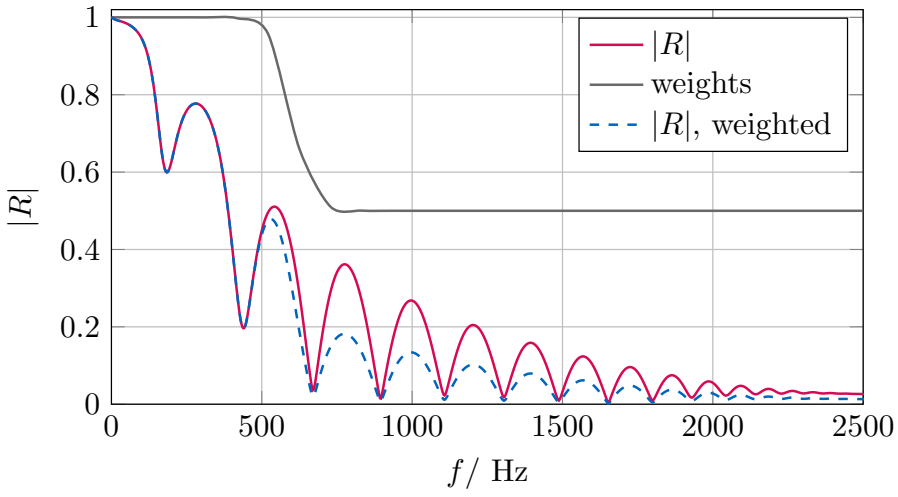

Figure 4.9: Influence of weighting on the reflection coefficient curve

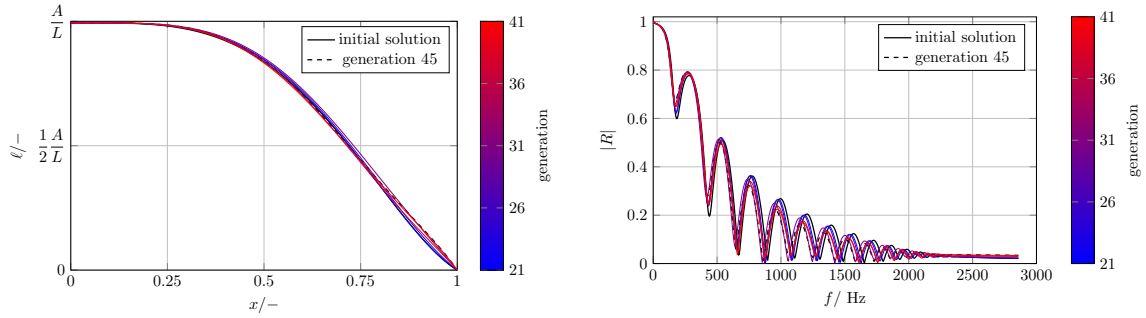

(a) (b)

Figure 4.10: Optimization progress with 7 control points: (a) ribs-height function ℓ, (b) reflection coefficient R

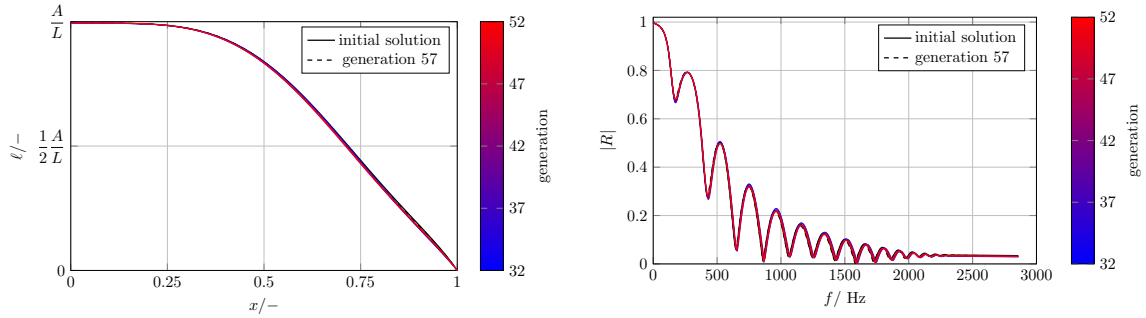

(a) (b)

Figure 4.11: Optimization progress with 8 control points: (a) ribs-height function ℓ, (b) reflection coefficient R

4.3.6 Run 6 with 8 control points

As the result of the previous run with seven control points was an improvement, its optimum will be used after degree elevation as an initial solution for this run. The weighting of the reflection coefficient is the same as in the previous run, given by eq. (4.5).

The first offspring better than the initial solution appeared in generation 32 and in generation 57 the evolution resulted in optimum (0.14909, 0.14909, 0.14909, 0.14905, 0.14897, 0.11292, 0.04382, 0.04179). Even though the evolution was running for 59 generations, the result is not distinctly different to the initial solution.

4.3.7 Conclusion of the optimization progress

As the further optimization did not lead to significantly better results, the optimal result from subsection 4.3.6 can be taken as the optimal solution for this setting. In the Figure 4.12 can be seen the overview of the optimization progress without the results of run 1 and run 4, which were not used.

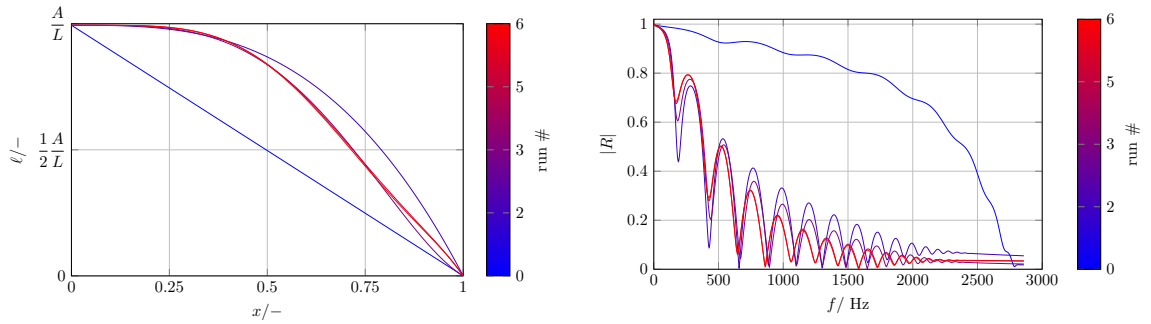

(a) (b)

Figure 4.12: Optimization progress (a) ribs-height function ℓ, (b) reflection coefficient R, from initial solution with linear ribs-height function ℓ (denoted as run 0) and parameters $A = 0.03$ m, $L = 0.2$ m, $W = 4$ mm, $\xi = 0.5$.

4.4 ABH optimization with quadratic initial solution

The second chosen initial solution ribs-height function ℓ is a quadratic function given by eq. (4.2) with $\ell_0 = 0.9905$ and Bézier control points (0.14858, 0.14929), see Figure 4.1b. From the results of section 4.3, we can possibly expect that the quadratic ribs-height function may ensure faster convergence. The reflection coefficient is evaluated for the same number of frequencies as in section 4.3

4.4.1 The process of optimization

In optimization with 3 control points, the result converged to the given boundaries (similarly as in subsection 4.3.1), and thus was not used in the next run.

With 4 control points and initial solution given as (0.14858, 0.14893, 0.12429, 0.07464), there is a noteworthy quick improvement from generation 1 to generation 21, see Figure 4.13. Then the progress is slowed down and the best reflection coefficient curves between generations become similar to each other. The best result (0.14909, 0.14909, 0.14909, 0.10956) is achieved in generation 34.

This best result was reused and extended by one control point to get the initial solution (0.14909, 0.14909, 0.14909, 0.13328, 0.08765). Since generation 14, the evolution began to improve and in generation 36 the best result was achieved. Although the overall reflection coefficient curve performs better than the initial guess, note, that in fact, it does not get better in the frequency range (1, 500) Hz.

Because of this problem, the result of optimization with 5 control points was not taken into account, and the evolution was restarted with 6 control points, which resulted in an almost identical reflection coefficient curve. Hence, the next evolution will be restarted with the same initial solution together with 7 control points.

With 7 control points, the best result (0.14909, 0.14909, 0.14909, 0.14900, 0.14593, 0.04170, 0.03560) was achieved in generation 43. Again, the reflection coefficient does not get better until cca 500 Hz, but at least it does not get significantly worse (see Figure 4.14).

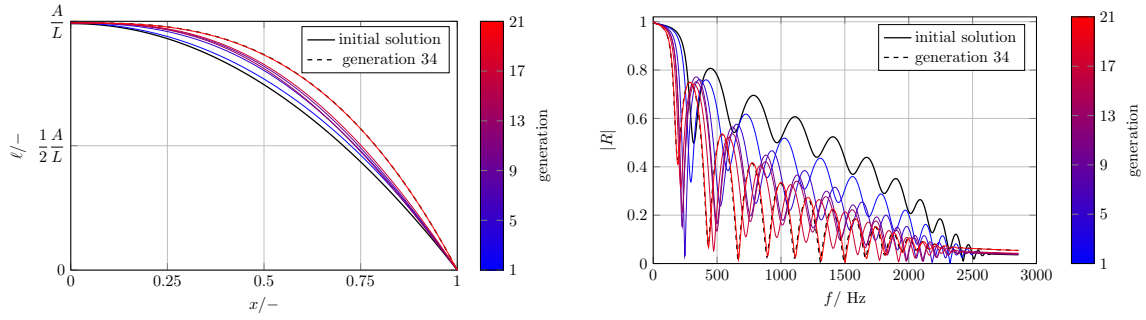

(a) (b)

Figure 4.13: Optimization progress with 4 control points: (a) ribs-height function ℓ, (b) reflection coefficient R

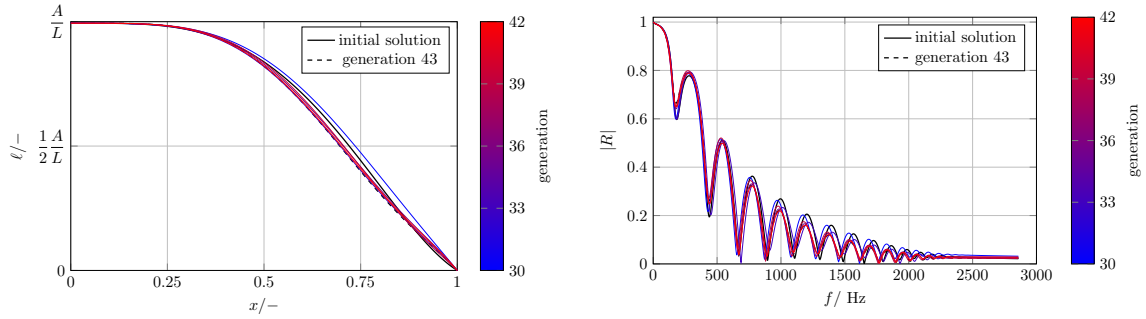

(a) (b)

Figure 4.14: Optimization progress with 7 control points: (a) ribs-height function ℓ, (b) reflection coefficient R

In restart with 8 control points, a result of the last evolution was used as the initial solution. For comparison, the result of this evolution was compared to the result of evolution with the weighted cost function emphasizing the lower frequencies, given by eq. (4.5). Because the evolution with the weighted cost function is better in terms of the reflection coefficient spectrum in the frequency band (1, 950) Hz, its result will be taken into account and used for the next restart.

4.4.2 Conclusion of the optimization progress

The restart with 9 control points did not lead to any significant improvement, moreover, it would not be wise to continue with elevating the degree of the Bézier curve and proceed further with evolution in order to get better results. Therefore, the result of optimization with 8 control points will be considered as the overall best solution of this whole optimization with the quadratic initial solution. The overview of the optimization progress can be seen in Figure 4.15, the optimum reached in this sequence is (0.14909, 0.14909, 0.14909, 0.14900, 0.14816, 0.11296, 0.04702, 0.03975).

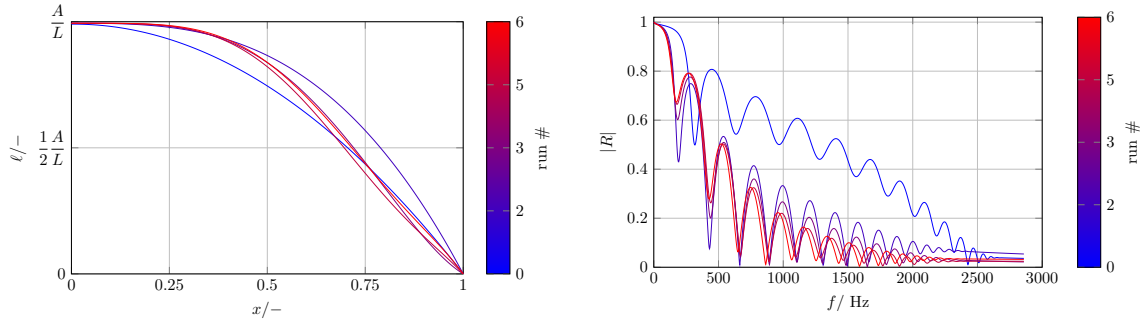

(a) (b)

Figure 4.15: Optimization progress (a) ribs-height function ℓ, (b) reflection coefficient R, from initial solution with quadratic ribs-height function ℓ (denoted as run 0) and parameters $A = 0.03$ m, $L = 0.2$ m, $W = 4 \cdot 10^{-3}$ m, $\xi = 0.5$.

4.5 Comparison of the results

Firstly, we can conclude from the results, that three control points for the ribs-height function ℓ given by the Bézier curve do not provide enough degrees of freedom, as they repeatedly resulted in a bounded optimum.

The most important fact is, that in both described cases of evolution, even though the Bézier control points themselves slightly differ, the resulting ribs-height functions ℓ and the reflection coefficient curves are identical, as can be seen in Figure 4.16. This means, that the optimization was set properly.

However, contrary to the hypothesis, the speed of convergence to the optimum is not so different if the linear or quadratic initial solution is used.

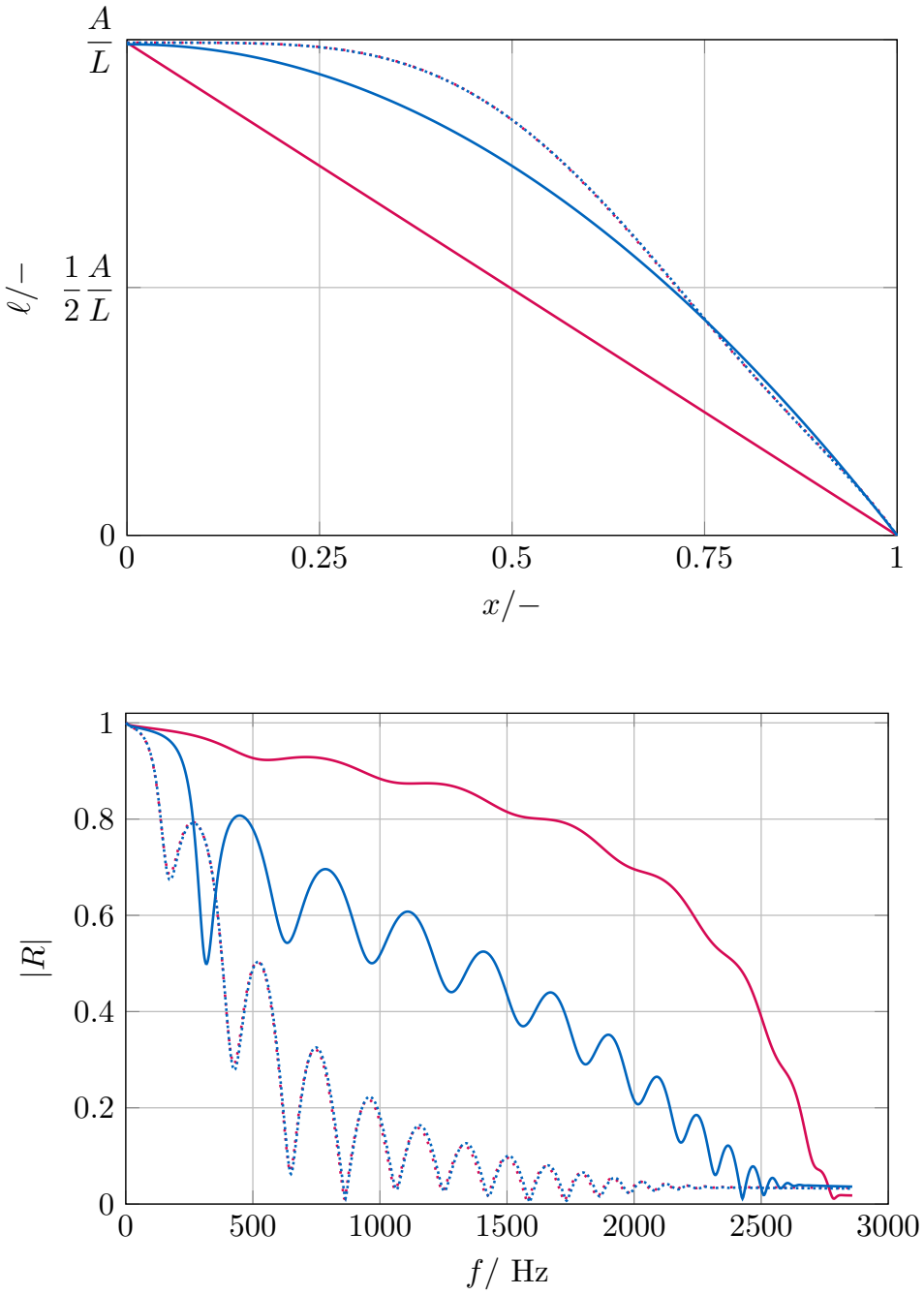

Figure 4.16: Comparison of the evolution results from the linear and quadratic initial solution, where the red, blue, dotted red, dotted blue line signify linear initial solution, quadratic initial solution, the result of optimization with linear initial solution and result of optimization with quadratic initial solution, respectively. Top: ribs-height function ℓ, bottom: reflection coefficient spectra R

Chapter 5

Optimization of ABH with use of a porous material

Throughout this chapter, the improvement of sound absorption in ABH with use of a porous material is studied. The benchmark for optimization is introduced in section 5.1. In section 5.2 and section 5.3 the optimization process is described with emphasis on used cost functions. Finally, in section 5.4, the results of optimization with two different ways of porous material insertion are compared.

5.1 Benchmarks

In this chapter, our goal is to improve the sound absorption of the porous material using the ABH. Hence, we decided for one of the usual uses of porous materials as a benchmark, namely for the waveguide termination in the length of a quarter-wavelength resonance at the Biot's frequency [25]

$$f_{\text{Biot}} = \frac{\sigma\phi}{2\pi\rho_0\alpha_\infty}\,, \tag{5.1}$$

where σ, ϕ, ρ_0, α_∞ are the flow resistivity, porosity, the density of the saturating fluid and tortuosity, respectively. This frequency represents the transition frequency between two regimes of thermoviscous losses, particularly the viscous and inertial regime. Since the porous material in the inertial regime can efficiently absorb the sound, we will focus on the viscous regime. Therefore, our goal is to improve the sound absorption of the porous material in the frequency region below Biot's frequency.

The parameters of chosen porous material are following: flow resistivity $\sigma = 5678$ $\mathrm{Pa\,s\,m^{-2}}$, porosity $\phi = 0.99$, tortuosity $\alpha_\infty = 1$, static viscous permeability $\kappa_0 = 3.1877 \times 10^{-9}$ $\mathrm{m^2}$, static thermal permeability $\kappa_0' = 4.5866 \times 10^{-9}$ $\mathrm{m^2}$, thermal and viscous characteristic lengths $\Lambda' = 244$ µm and $\Lambda = 147$ µm, respectively. Thus, the Biot's frequency of chosen material is $f_{\text{Biot}} = 752$ Hz and the corresponding length of a quarter wavelength resonator at the Biot's frequency is $L_p = 0.114$ m. The absorption of this particular porous material at length $L_p = 0.114$ m is depicted in Figure 5.1.

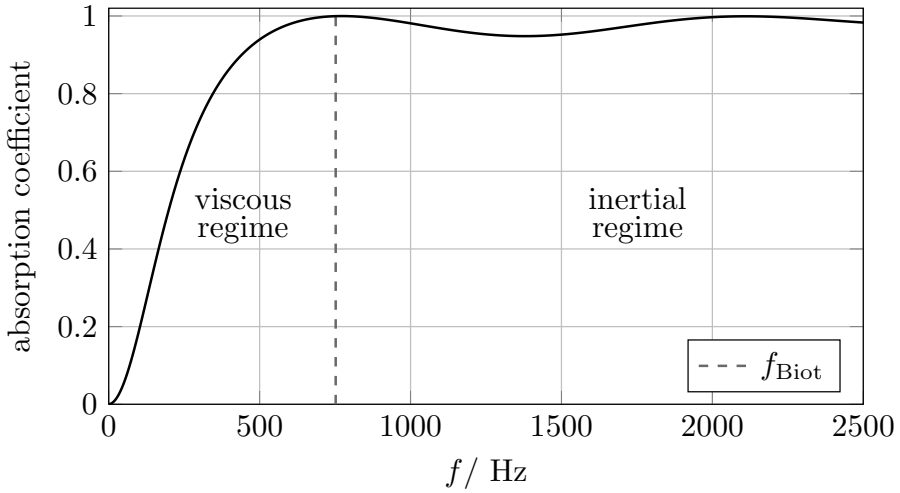

Figure 5.1: Absorption coefficient of the given benchmark.

5.2 ABH terminated by a porous material

In this case, we consider porous termination at a length corresponding to the quarter-wavelength resonance at the Biot's frequency, i.e., $L_p = 0.114$ m and the impedance matching is done by ABH of length $L = 0.15$ m and half-height $A = 0.03$ m. Other parameters used for the optimization with this configuration are $W = 4$ mm and $\xi = 0.5$.

Note, that due to the pore size and the assumptions for using the macro-scale model, the area exposed to the incident wave should be at least 5 mm high. The initial solution, quadratic ribs-height function ℓ with $\ell_0 = 0.9165$, is given by control points (0.18330, 0.18887, 0.12777). The ribs-height function ℓ and absorption coefficient of the initial solution can be seen in Figure 5.2.

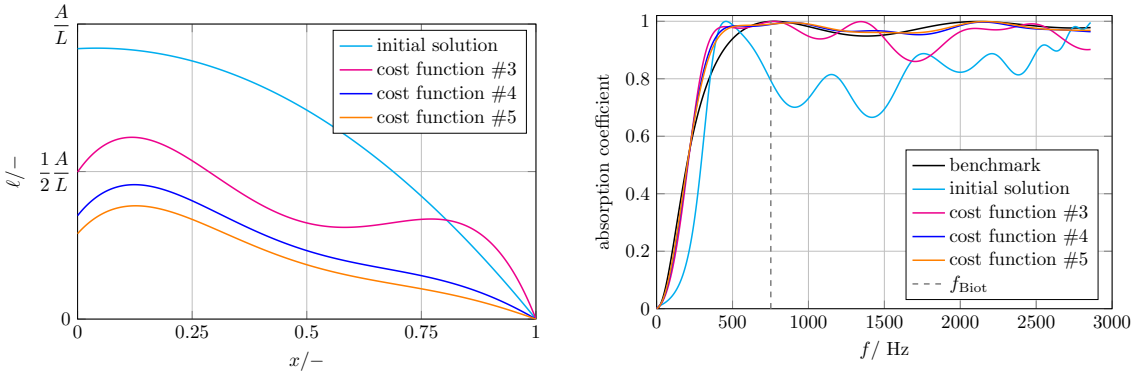

(a) (b)

Figure 5.2: Absorption coefficient for the ABH terminated by a porous material, optimal results given by cost functions #3, #4, #5

#n	cost function	interpretation
#1	$-\int_0^{f_{\text{cut}}} \alpha(f)\mathrm{d}f$	maximization of absorption coefficient, minus in order to maintain the minimization framework
#2	$\int_0^{f_{\text{cut}}} [\alpha_{\text{benchmark}}(f) - \alpha(f)]\,\mathrm{d}f$	comparison with the benchmark
#3	$\int_0^{f_{\text{Biot}}} [\alpha_{\text{benchmark}}(f) - \alpha(f)]\,\mathrm{d}f$	comparison with the benchmark in the viscous regime only
#4	cost function #2 + cost function #3	cost function #2, #3 combined
#5	$\int_0^{f_{\text{cut}}} [\alpha_{\text{reference}}(f) - \alpha(f)]\,\mathrm{d}f$	comparison with the reference (depicted Figure 5.3), given as the benchmark absorption coefficient in the viscous regime and a sigmoid function in the inertial regime

Table 5.1: Table of cost functions for the optimization of ABH with use of a porous material.

For the optimization of ABH terminated by a porous material, five cost functions were proposed, see Table 5.1. The meaning of the simplest cost function #1 is the maximization of absorption coefficient. In order to maintain the minimization framework, instead, the negative absorption is minimized.

However, cost function #1 does not take into account the absorption coefficient of the benchmark, which we are trying to outperform. Hence, a second cost function, cost function #2 was proposed in the form of minimizing the difference between the benchmark and the offsprings. In fact, the optimization with cost function #1 and #2 for ABH terminated by a porous material resulted in the same ribs-height function ℓ. A hypothesis was, that the cost function #2 does not emphasize the viscous regime enough; therefore cost function #3 was proposed as minimization of the difference between offsprings and the benchmark only in the viscous regime (i.e., only in the frequency range below the Biot's frequency).

In fact, the results of cost function #1 and #2 for ABH terminated by a porous material were the same. Even though the result of cost function #3 in the viscous regime is better than the result of the previous two cost function, due to the performance in the inertial regime, this result is much worse than the benchmark.

This problem was solved by a cost function #4, proposed in the form of a sum of cost functions #2 and #3. As seen in Figure 5.2, the optimized result outperforms the benchmark in the viscous regime and the performance in the inertial regime is comparable with the

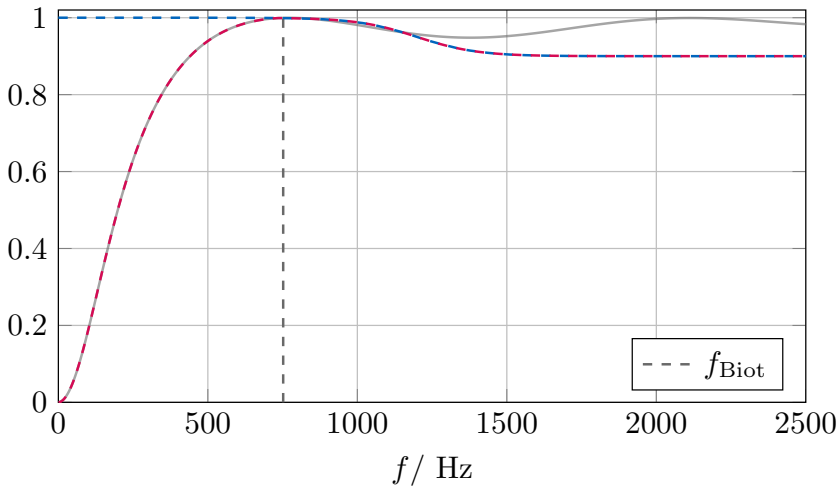

Figure 5.3: The grey solid line signifies the absorption coefficient curve of the given benchmark, the blue dashed line is for the sigmoid function and the red dashed line depicts the adapted reference, which is the combination of the absorption coefficient curve (in the frequency range [1, f_{cut}] Hz) and the sigmoid function (in the frequency range [f_{Biot}, f_{cut}] Hz).

benchmark. Since our aim is not to outperform the porous material in the inertial regime, rather it is sufficient to reach, e.g. 90 % of absorption, a new reference was defined. Then, the cost function #5 is defined as minimizing the difference between the new reference (which can be seen in Figure 5.3) and the offsprings. The new reference consists in the viscous regime of benchmark absorption coefficient and in the inertial regime of a sigmoid function depicted in Figure 5.3. Surprisingly, the result of optimization using the cost function #5 was the same as the results of cost function #1 and #2.

The achieved optimal results for cost functions can be seen in Table 5.2. The optimizations with cost functions #1, #2 and #5 resulted in the same solutions. The optimal solution for this configuration will be considered the result of optimization with the use of cost function #4. For the optimal geometry see Figure 5.4.

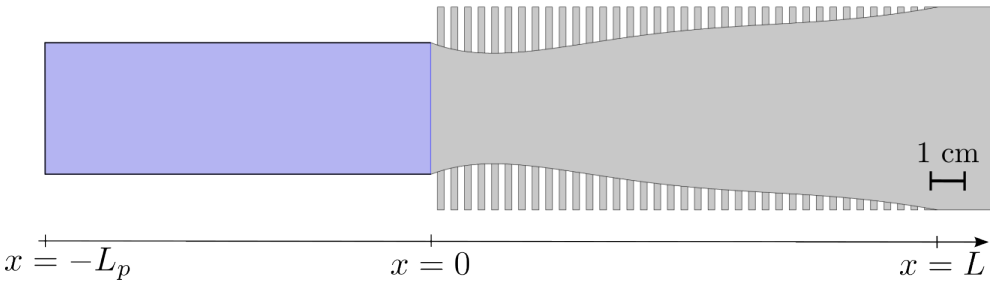

Figure 5.4: Optimal geometry for the considered rectangular ABH terminated by a porous material (marked in blue).

cost function #n	result
#1	(0.05796, 0.12699, 0.00000, 0.03789, 0.02197)
#2	(0.05799, 0.12708, 0.00000, 0.03801, 0.02198)
#3	(0.09969, 0.18998, 0.02504, 0.13499, 0.15811)
#4	(0.07012, 0.14838, 0.00000, 0.04942, 0.03582)
#5	(0.05792, 0.12690, 0.00000, 0.03775, 0.02189)

Table 5.2: Table of achieved optimal control points for different cost functions for ABH terminated by a porous material.

5.3 ABH with slits filled by porous material

For this configuration, ABH with slits filled with porous material and rigid wall termination, the length of ABH is $L = 0.15$ m and the half-height is $A = 0.03$ m. As was mentioned in section 5.2, the area exposed to the incident wave should be for the used porous material at least 5 mm wide. Hence, the width of slit w was set as $w = 5$ mm. The width of slits remains the same (2 mm) and thus, the spatial period of ribs is $W = 7$ mm and the rib-width to slit ratio is $\xi = 5/7$. The initial solution, quadratic ribs-height function ℓ with $\ell_0 = 0.9905$, is given by control points (0.14858, 0.14905, 0.09953). The ribs-height function ℓ and absorption coefficient of the initial solution can be seen in Figure 5.5.

Although in the case of ABH terminated by a porous material the performance of mentioned cost functions differed, for this configuration, the results were almost identical. The final result (depicted in Figure 5.6) was obtained with the use of cost function #3. Note, that none of the optimal solutions used the partial filling of slits with porous material. In all optimal cases, whole slits were filled by the porous material.

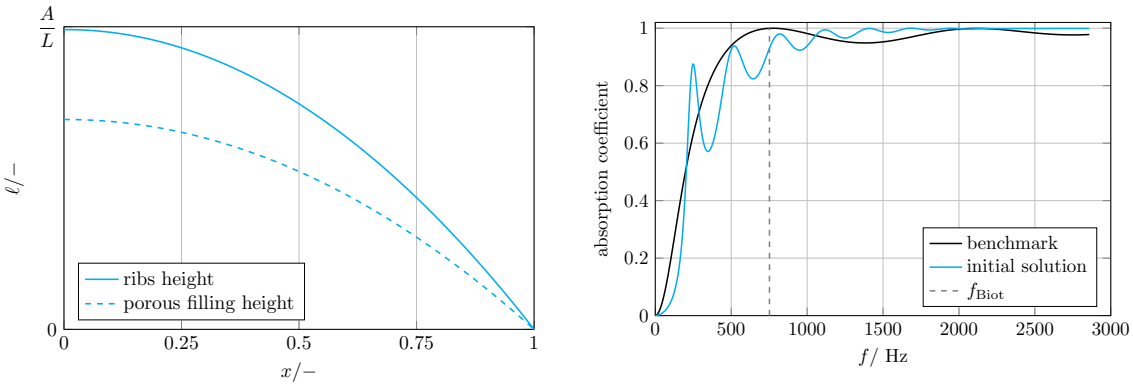

(a) (b)

Figure 5.5: The initial solution for ABH with slits filled with porous material, (a) the ribs-height function ℓ and the height of porous material filling, (b) the absorption coefficient of the initial solution.

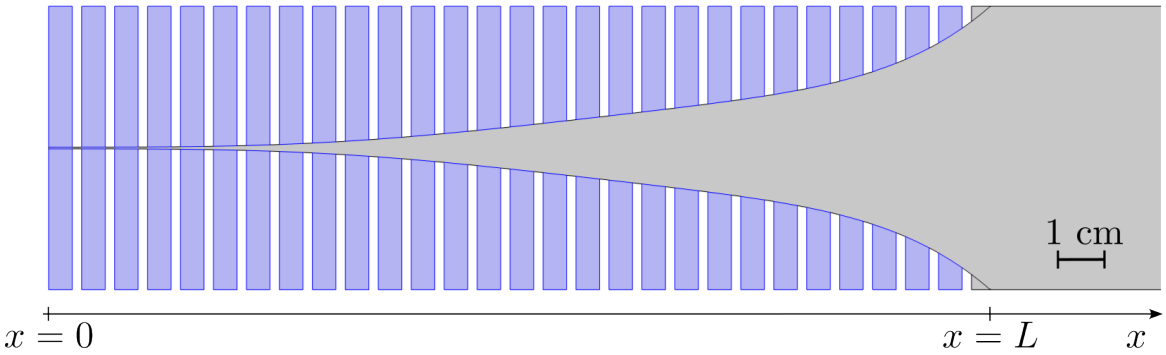

Figure 5.6: Optimal geometry for the considered rectangular ABH terminated by a perfectly rigid wall, with slits filled by a porous material (marked in blue).

5.4 Results

In this chapter, two possible ways of employing the porous material within the ABH were studied. We have focused on absorption in the viscous regime of the porous material, trying to beat the chosen benchmark: the waveguide termination by the porous material with a thickness corresponding to a quarter wavelength resonator at the Biot's frequency.

In the case of ABH terminated by a porous material, leaving the ABH profile at $x = 0$ wide open is clearly advantageous, as there is a large area of porous material exposed to the incident wave with a rather moderate concentration of the wave energy due to the ABH shape. By utilizing the optimized design depicted in Figure 5.4, it is possible to achieve $\alpha > 0.9$ approximately 100 Hz earlier than the benchmark, see Figure 5.7. Even though the benchmark was outperformed, the improvement in sound absorption is not significant enough to outweigh the increase in overall length.

The optimal shape for ABH with slits filled by porous material is depicted in Fig. 5.6 and the corresponding absorption coefficient α in Figure 5.7. From 140 Hz, which corresponds to $\approx f_{\mathrm{Biot}}/5$, $\alpha > 0.7$ is already achieved. In Figure 5.8 the estimation of losses in different parts of ABH and for different frequencies is depicted. It is evident that the lower the frequency is, the closer to the closed end of the ABH is the sound energy of an incoming wave dissipated. As already noted in [8] for a similar case, the wave energy at higher frequencies does not even reach the closed end.

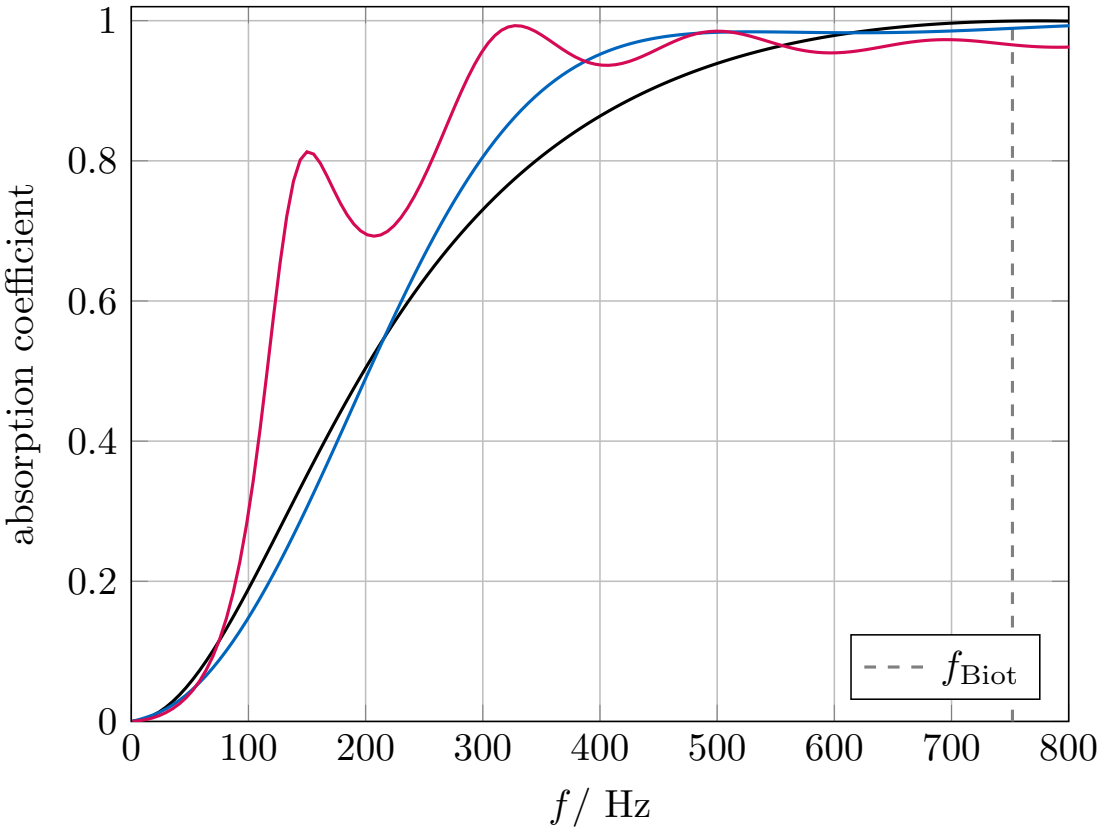

Figure 5.7: Comparison of optimization results of ABH with the use of a porous material. The black, blue and red lines depict the benchmark, the optimal solution for ABH terminated by a porous material and the optimal solution for ABH with slits filled by the porous material.

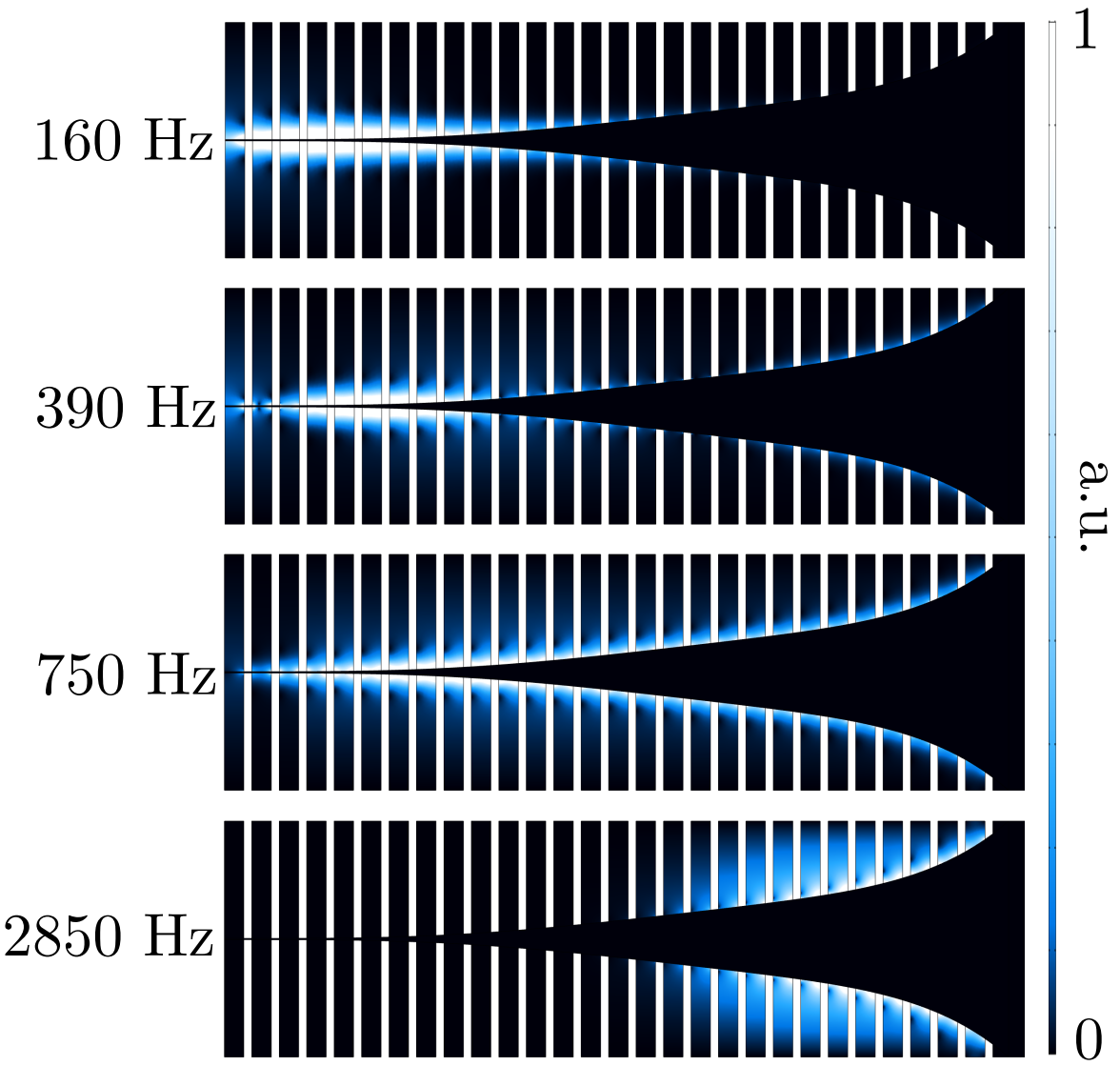

Figure 5.8: Estimation of power losses in slits filled with porous material at different frequencies. The depicted quantity is $-2|\boldsymbol{i}|\mathrm{Im}(k)$, where $|\boldsymbol{i}|$ and k denote the magnitude of the acoustic intensity vector and the complex wavenumber, respectively.

Chapter 6

Conclusions

In this thesis, the possibilities of optimizing the ABH geometry were investigated. The goal of this optimization was to maximize the absorption of incoming acoustic waves. Although there are numerous parameters that could be optimized since the ABH is usually a termination of a more complex device, most of the parameters are constrained in order to fit in geometry requirements and due to practical feasibility for 3D printing with the current state of development. Hence, it was decided to use the height of ribs as the subject of optimization because it is easy to control, optimize and fulfil practical requirements.

So far, the behaviour of ABHs with power-law profiles has been investigated. Our choice of the subject of optimization extends the possible geometries of ABHs. Thus, an appropriate parametrization of the ribs-height function ℓ was needed. The profile of ABH has to be a continuous, smooth, slowly varying curve. We have chosen a widely used parameterization for modelling smooth and continuous curves, known as the Bézier curve. One of the advantages of Bézier curves lies in the fact, that we can start the optimization with a lower amount of Bézier control points and restart the optimization with an increasing number of control points until convergence.

A suitable optimization algorithm had to be found because the relationship between the ribs-height function ℓ a and the reflection coefficient spectra is complicated. It is only known that the lower frequency waves tend to travel to the closed end of ABH. The higher the frequency of the wave is, the closer to the open end of ABH the sound energy of an incoming wave is dissipated [8]. Therefore, we decided to use a derivative-free optimization, namely the optimization algorithm Covariance Matrix Adaptation Evolution Strategy. The optimization algorithm for the purpose of optimizing sound absorption in rectangular ABHs was implemented using the open-source Python library for CMA Evolution Strategy [22]. The governing equations and the Bézier curve parametrization of the ribs-height function ℓ were implemented in Python using libraries NumPy [20] and SciPy [21].

Firstly, a rigidly backed ABH was studied. ABHs mostly serve as an anechoic waveguide termination. As this concept does not employ a porous material, they can be used in extreme conditions (high temperatures, humidity, etc.) or in conditions with increased hygiene standards (healthcare industry). The reached optimal ribs-height function ℓ differs from those studied in previous works [2] and offers efficient sound absorption.

Secondly, since the use use of ABHs can significantly improve sound absorption in a frequency range below the Biot's frequency of the porous material, two possible ways of

employing the porous material within the ABH were studied. We have focused on absorption in the viscous regime of the porous material, trying to beat the chosen benchmark: the waveguide termination by the porous material with a thickness corresponding to a quarter wavelength resonator at the Biot's frequency. The benchmark was outperformed in the case of ABH terminated by a porous material. However, the overall improvement in sound absorption is not significant enough to outweigh the increase in overall length. Fortunately, the optimal solution for ABH with slits filled with porous material was more successful. We have extended the frequency range of efficient absorption. Specifically, the absorption $\alpha > 0.7$ is achieved already for the frequency corresponding to $\approx f_{\text{Biot}}/5$. The results are depicted in Figure 6.1.

In the future, even if we do not account for the possibility of further 3D printing evolution, other parameters than the ribs-height function ℓ could be optimized. Within the limits of practical feasibility, we suggest optimizing the spatial period of ribs W or possibly the rib-width to slit ratio ξ as a function of the location in the ABH, i.e., $W = W(x)$ and $\xi = \xi(x)$. In addition, more types of porous materials (foams, felts, straws etc.) can be considered for optimization.

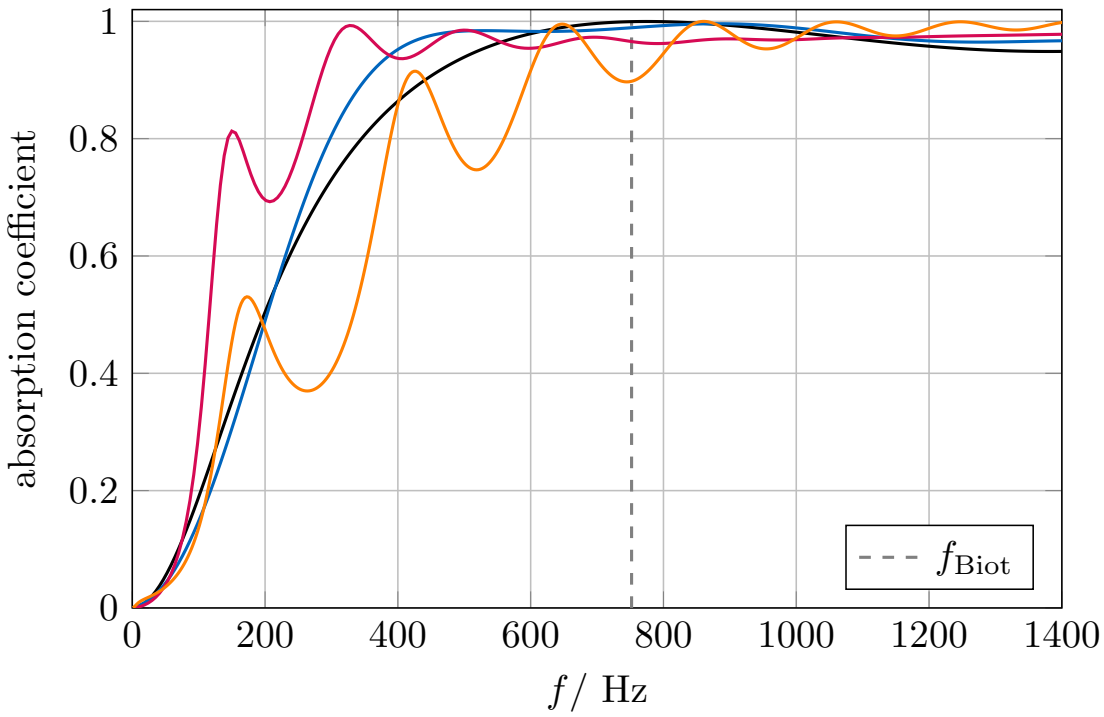

Figure 6.1: Absorption coefficient of optimized solutions. The orange line depicts the optimal solution for the ABH terminated by a rigid wall. The black, blue and red lines depict the benchmark, the optimal solution for ABH terminated by a porous material and the optimal solution for ABH with slits filled by the porous material. Depicted frequency range is from 0 Hz to frequency corresponding to $\approx f_{\text{cut}}/2$ of the ABH.

Bibliography

[1] European Environment Agency. *Environmental noise in Europe, 2020.* Publications Office, 2020. DOI: 10.2800/686249.

[2] Adrien Pelat et al. "The acoustic black hole: A review of theory and applications". In: *Journal of Sound and Vibration* 476 (2020), p. 115316. ISSN: 0022-460X. DOI: 10.1016/j.jsv.2020.115316.

[3] M. A. Mironov and V. V. Pislyakov. "One-dimensional acoustic waves in retarding structures with propagation velocity tending to zero". In: *Acoustical Physics* 48 (2002), pp. 347–352. DOI: 10.1134/1.1478121.

[4] Abdelhalim Azbaid El Ouahabi, Victor Krylov, and Dan O'Boy. "Experimental investigation of the acoustic black hole for sound absorption in air". In: *22nd International Congress on Sound and Vibration, Florence, Italy*. July 2015.

[5] Abdelhalim Azbaid El Ouahabi, Victor Krylov, and Dan O'Boy. "Investigation of the acoustic black hole termination for sound waves propagating in cylindrical waveguides". In: *International Conference 'InterNoise 2015', San Francisco, USA*. Aug. 2015.

[6] Mikhail Mironov and Vladimir Pislyakov. "One-dimensional sonic black holes: Exact analytical solution and experiments". In: *Journal of Sound and Vibration* 473 (May 2020), p. 115223. DOI: 10.1016/j.jsv.2020.115223.

[7] Yongzhen Mi et al. "Wave trapping by acoustic black hole: Simultaneous reduction of sound reflection and transmission". In: *Applied Physics Letters* 118.11 (Mar. 2021), p. 114101. DOI: 10.1063/5.0042514.

[8] M. Červenka and M. Bednařík. "On the role of resonance and thermoviscous losses in an implementation of "acoustic black hole" for sound absorption in air". In: *Wave Motion* 114 (2022), p. 103039. ISSN: 0165-2125. DOI: 10.1016/j.wavemoti.2022.103039.

[9] Olga Umnova et al. "Multiple resonances in lossy acoustic black holes - theory and experiment". In: *Journal of Sound and Vibration* 543 (Jan. 2023), p. 117377. DOI: 10.1016/j.jsv.2022.117377.

[10] David T. Blackstock. *Fundamentals of physical acoustics*. Wiley, 2000, p. 422. ISBN: 978-0-471-31979-5.

[11] Abbas Mousavi, Martin Berggren, and Eddie Wadbro. "How the waveguide acoustic black hole works: A study of possible damping mechanisms". In: *The Journal of the Acoustical Society of America* 151.6 (June 2022), pp. 4279–4290. DOI: 10.1121/10.0011788.

[12] Oriol Guasch, Marc Arnela, and Patricia Sánchez-Martín. "Transfer matrices to characterize linear and quadratic acoustic black holes in duct terminations". In: *Journal of Sound and Vibration* 395 (2017), pp. 65–79. ISSN: 0022-460X. DOI: 10.1016/j.jsv.2017.02.007.

[13] Neha Sharma, O. Umnova, and Andy Moorhouse. "Low frequency sound absorption through a muffler with metamaterial lining". In: *24th International Congress on Sound and Vibration 2017*. July 2017.

[14] L. De Ryck et al. "Reconstruction of material properties profiles in one-dimensional macroscopically inhomogeneous rigid frame porous media in the frequency domain". In: *The Journal of the Acoustical Society of America* 124.3 (Sept. 2008), pp. 1591–1606. DOI: 10.1121/1.2959734.

[15] Michael R. Stinson. "The propagation of plane sound waves in narrow and wide circular tubes, and generalization to uniform tubes of arbitrary cross-sectional shape". In: *The Journal of the Acoustical Society of America* 89.2 (1991), pp. 550–558. DOI: 10.1121/1.400379.

[16] Noé Jiménez, Jean-Philippe Groby, and Vicent Romero-García. "The Transfer Matrix Method in Acoustics". In: *Acoustic Waves in Periodic Structures, Metamaterials, and Porous Media: From Fundamentals to Industrial Applications*. Ed. by Noé Jiménez, Olga Umnova, and Jean-Philippe Groby. Cham: Springer International Publishing, 2021, pp. 103–164. ISBN: 978-3-030-84300-7. DOI: 10.1007/978-3-030-84300-7_4.

[17] Ingo Rechenberg. "Evolutionsstrategie : Optimierung technischer Systeme nach Prinzipien der biologischen Evolution". In: 1973.

[18] Nikolaus Hansen. *The CMA Evolution Strategy: A Tutorial*. 2016. DOI: 10.48550/arXiv.1604.00772. URL: <https://arxiv.org/abs/1604.00772v2>.

[19] Sentewolf. *Concept of directional optimization in CMA-ES algorithm*. 2016. URL: <https://commons.wikimedia.org/wiki/File:Concept_of_directional_optimization_in_CMA-ES_algorithm.png>. Accessed 20-Dec-2022.

[20] Charles R. Harris et al. "Array programming with NumPy". In: *Nature* 585.7825 (Sept. 2020), pp. 357–362. DOI: 10.1038/s41586-020-2649-2.

[21] Pauli Virtanen et al. "SciPy 1.0: Fundamental Algorithms for Scientific Computing in Python". In: *Nature Methods* 17 (2020), pp. 261–272. DOI: 10.1038/s41592-019-0686-2.

[22] Masashi Shibata and Masahiro Nomura. *Lightweight Covariance Matrix Adaptation Evolution Strategy (CMA-ES) implementation for Python 3*. URL: <https://pypi.org/project/cmaes/>. Accessed 17-Mar-2023.

[23] Henrik Møller and Christian Pedersen. "Hearing at low and infrasonic frequencies". In: *Noise & health* 6 (Apr. 2004), pp. 37–57.

[24] *3d printers | original prusa 3d printers directly from josef prusa*. URL: <https://www.prusa3d.com/category/3d-printers/>. Accessed 1-Apr-2022.

[25] Jean-Philippe Groby, Noé Jiménez, and Vicent Romero-García. "Acoustic Metamaterial Absorbers". In: *Acoustic Waves in Periodic Structures, Metamaterials, and Porous Media: From Fundamentals to Industrial Applications*. Ed. by Noé Jiménez, Olga Umnova, and Jean-Philippe Groby. Cham: Springer International Publishing, 2021, pp. 167–204. ISBN: 978-3-030-84300-7. DOI: 10.1007/978-3-030-84300-7_5.

Appendix A

List of Abbreviations

ABH	Acoustic Black Hole
CMA-ES	Covariance Matrix Adaptation Evolution Strategy
FEM	Finite Element Method
JCAL	Johnson-Champoux-Allard-Lafarge
LNSE	Linearized Navier-Stokes Equations

Appendix B

Contents of attached CD

The organization of files on CD attached to this thesis can be seen below. The zip archive `source_code.zip` consists of three python files. File `evolution.py` contains one main function, which controls the evolution and where the initial conditions for evolution can be set. In `cost_function.py`, the cost function for evolution is implemented together with other functions made for saving and displaying the results during the evolution. Lastly, in `abh_functions.py`, the governing equations for ABHs and porous materials are implemented.